International Journal of Heat and Mass Transfer 253 (2025) 127599

Contents lists available at ScienceDirect

International Journal of Heat and Mass Transfer

journal homepage: www.elsevier.com/locate/ijhmt

Multi-phase flow and heat transfer characteristics of composite heat storage materials during melting process: simulation and optimization

Xinyu Huang [a], Yuan Xie [a], Yuanji Li [a], Haichuan Luo [c], Jie Xue [c], Xiaohu Yang [a,b,*], Hussam Jouhara [d,e,*]

[a] Institute of the Building Environment & Sustainability Technology, School of Human Settlements and Civil Engineering, Xi'an Jiaotong University, Xi'an 710049, PR China
[b] Key Laboratory of Thermo-Fluid Science and Engineering of Ministry of Education, School of Energy and Power Engineering, Xi'an Jiaotong University, Xi'an, Shaanxi 710049, PR China
[c] China Northwest Architecture Design and Research Institute, Co., Ltd., Xi'an 710061, PR China
[d] Heat Pipe and Thermal Management Research Group, College of Engineering, Design and Physical Sciences, Brunel University London, UB8 3PH, UK
[e] Vytautas Magnus University, Studentu Str. 11, LT-53362 Akademija, Kaunas Distr., Lithuania

ARTICLE INFO

Keywords:
Phase change material
Two-phase flow
Flow heat transfer
Natural convection
Melting properties
Optimization prediction

ABSTRACT

The low thermal conductivity of phase change materials (PCMs) has limited their large-scale energy storage applications. This paper focuses on the rapid heat storage process of phase change energy storage. A composite heat storage structure is proposed, in which 50 % of solid-PCMs are filled at the bottom and water is at the top. During the melting process, heat is continuously exchanged through the mixture of water and liquid PCM to enhance heat transfer. A computational model (Case 1) is established using the computational fluid dynamics-volume of fluid (CFD-VOF) numerical method and compared with the Case 0 structure with 50 % water at the bottom. The reliability of the numerical model is verified through experiments, and the two-phase flow state of wax and PCM in the Case 1 structure is observed. Further, through numerical studies, the liquid phase evolution, temperature distribution, and internal flow velocity during the heat transfer process of different composite melting structures were analyzed, and the melting performance and energy storage performance were quantitatively evaluated. In addition, the melting characteristics of this novel energy storage structure at different wall temperatures are discussed in detail. The results show that compared with Case 0, the melting time of PCM in Case 1 is shortened by 51.75 %, while the average velocity of PCM and the average velocity of water are increased by 100.75 % and 67.33 % respectively, compared with Case 0. However, compared with Case 0, the total heat storage capacities of PCM and water in Case 1 are reduced by 3.17 % and 19.27 % respectively. Finally, the response surface method is used to optimize and predict the comprehensive heat storage rate and heat storage time, and the accuracy of the optimization results exceeds 98.995 %.

1. Introduction

Energy storage technology plays a critical role in facilitating the efficient utilization and widespread adoption of renewable energy sources [1]. By addressing the challenges associated with the volatility and intermittency of renewable energy, energy storage systems can effectively balance power supply and demand, enhance energy utilization efficiency, and diminish reliance on traditional fossil fuels [2,3]. Among the various energy storage technologies, thermal energy storage (TES) is a significant component [4,5]. Its extensive applications in power generation, heating, and industrial waste heat recovery contribute to the decarbonization of energy systems, thereby providing substantial technical support for global energy transformation initiatives [6,7].

Among various TES technologies, phase change energy storage is a method that capitalizes on the ability of materials to absorb or release significant amounts of latent heat to store and release energy during phase transitions [8,9]. This technology offers advantages such as high energy density and stable temperature, making it widely applicable in areas such as building energy efficiency, cooling of electronic equipment, industrial waste heat recovery, and solar energy utilization [10,11]. However, many phase change materials (PCMs), particularly organic materials, exhibit poor thermal conductivity, resulting in low

* Corresponding authors.
E-mail addresses: xiaohuyang@xjtu.edu.cn (X. Yang), Hussam.Jouhara@brunel.ac.uk (H. Jouhara).

https://doi.org/10.1016/j.ijheatmasstransfer.2025.127599
Received 18 June 2025; Received in revised form 15 July 2025; Accepted 23 July 2025
Available online 29 July 2025

Nomenclature

Abbreviation

TES	Thermal energy storage
PCM	phase change material
VOF	Volume of Fluid
UDF	User - Defined Function
CFD	Computational Fluid Dynamics

Symbols

a	volume fraction
A_{mush}	paste region constant
C_d	drag coefficient
c_p	isobaric specific heat
f	liquid fraction
k	thermal conductivity (W/m·K)
H	total enthalpy
h_{ref}	sensible enthalpy
$\dot{f}$	melting rate
$\vec{F}$	drag forces
$\vec{g}$	acceleration of gravity
$T_{liquidus}$	liquidus temperature (K)
$T_{solidus}$	solidus temperature (K)
T_m	melting temperature (K)
Q_{ext}	external heat source
$Q_{gen}^{w-p}, Q_{gen}^{p-w}$	heat exchange terms between water and paraffin.
T_c	current temperature (K)
T_i	initial temperature (K)
$\overline{q}$	average heat storage rate (W)
$\dot{q}$	instantaneous heat storage rate (W)
Q_{total}	total heat energy (J)
Q_l	latent heat energy (J)
Q_s	sensible heat energy (J)
Q_m	total heat absorbed at the end of melting (J)
t_m	total melting time
$\vec{u}$	flow rate
u, v	x direction velocity, y direction velocity

Greek symbols

λ	Latent heat of fusion (J/kg)
ρ	density (kg/m^3)
β	volumetric coefficient of thermal expansion (K^{-1})
μ	dynamic viscosity (Pa·s)
ε	decimal that prevents the denominator from being 0

Subscripts

i	initial
Ω	contact heat transfer interface
w	water
p	PCM

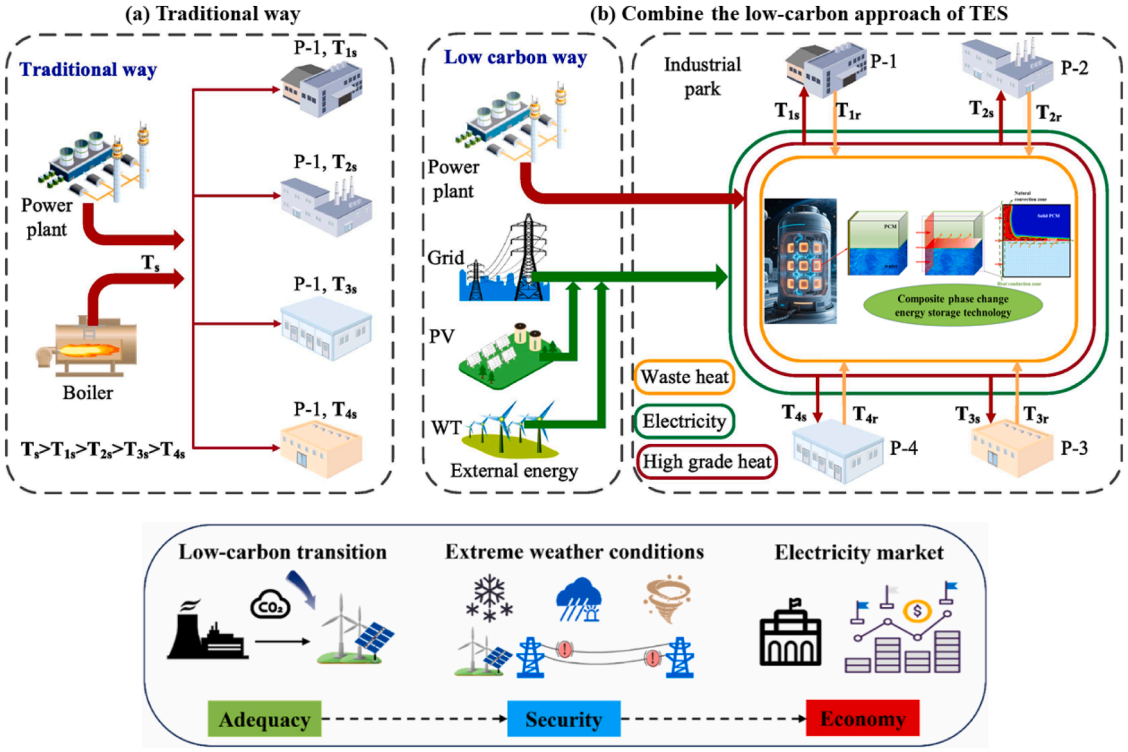

Fig. 1. Comprehensive energy utilization of traditional fossil fuel energy and renewable energy [40,41].

efficiency during phase changes. This limitation adversely affects the rapid storage and release of energy [12]. To enhance heat conduction properties of PCMs in practical applications, it is necessary to implement material modifications, such as incorporating high thermal conductivity materials, or to employ structural designs that include conductive media and optimized material layouts. As a result, the heat charging and discharging processes of PCMs have been the subject of extensive research. Additionally, researchers have identified the contact melting zone within the melting process, which presents significant advantages, including the elimination of additional energy consumption and compatibility with various vessel configurations. This advance is crucial for improving the heat charging and discharging rates associated with

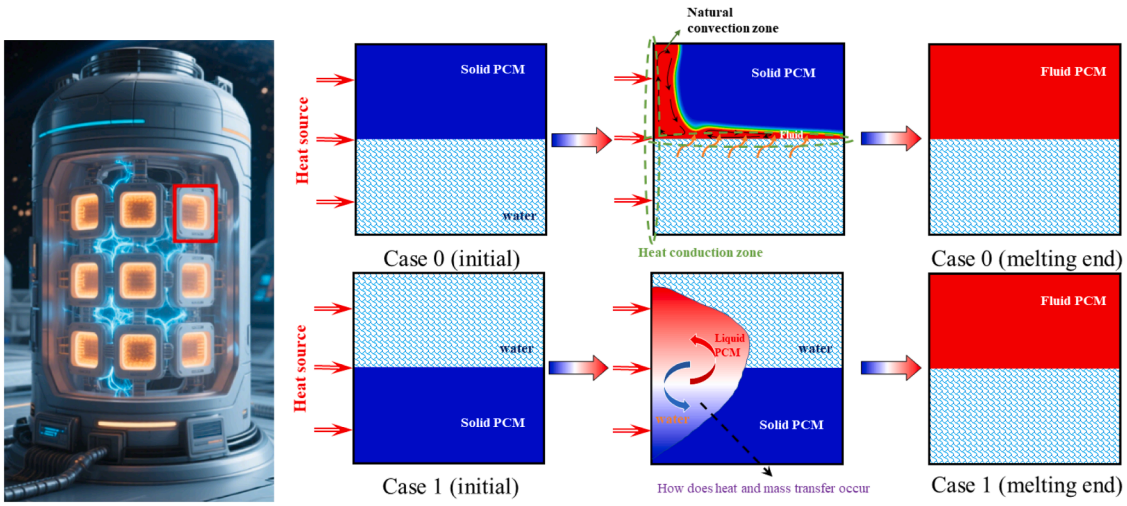

Fig. 2. Two modes of contact melting: Case 0 (water at the bottom initial) and Case 1 (solid state PCM initially at bottom).

Table 1
Thermophysical properties of substances [42,43].

Thermodynamic parameter	water	1-tetradecanol	Paraffin RT50	Cu	Unit
Density (ρ)	998.2	867.9 (solid) 818.8 (liquid)	880 (solid) 760 (liquid)	8978	kg/m^3
Thermal conductivity (k)	0.6	0.159	0.2	387.6	W/m·K
Isobaric specific heat (c_p)	4182	2360	2000	381	J/kg·K
Dynamic viscosity (μ)	0.001003	0.00212	0.0048	-	Pa·s
Volumetric coefficient of thermal expansion (β)	0.042	0.0011	0.0006	-	K^{-1}
Latent heat of fusion (λ)	334,000	227,800	168,000	-	J/kg
Liquidus temperature ($T_{liquidus}$)	273.15	315.15	324.15	-	K
Solidus temperature ($T_{solidus}$)	273.15	309.65	318.15	-	K
Melting temperature (T_m)	273.15	312.15	321.15	-	K

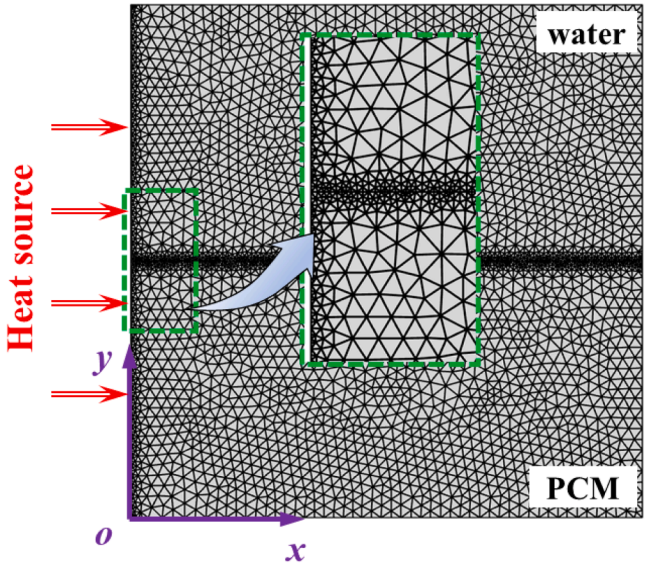

Fig. 3. Initial meshing in Case 1.

phase-change TES technology [13,14].

Contact melting describes the melting phenomenon where a heated surface and a solid surface to be melted maintain relative motion, resulting in the formation of a micro-liquid film for heat transfer under external forces. This process can be categorized into two modes: phase change material driving and heated surface driving [15,16].

Currently, researchers have conducted theoretical, experimental, and numerical investigations into contact melting within thermal energy storage units. Wilchinsky et al [17] developed a mathematical model to analyze the melting process of non-fixed materials in spherical and cylindrical heat storage units. They described the characteristic scales and dimensionless parameters associated with liquid flow and phase transition melting processes and examined the linearization of the Stefan number when there were slight differences between the densities of the solid-liquid phases. Their numerical solutions of the closed-form evolution equation demonstrated that the thickness of the melting layer decreases, and the melting rate diminishes, as the lower surface of the capsule becomes flatter. In a study by Zhao et al [18], contact melting was investigated within elliptic tubes with non-isothermal walls. They established a theoretical model to describe the variation of wall temperature with angle based on film theory and obtained a closed-form solution. Their findings revealed that, as the lengths and diameters of

Table 2
Solution method and difference scheme.

Object		Solution methods
Pressure-Velocity Coupling		SIMPLE Scheme
Spatial Discretization	Gradient	Least Squares Cell Based
	Energy	Second Order Upwind
	Volume Fraction	Geo-Reconstruct
	Momentum	Second Order Upwind
	Pressure	PRESTO!
Transient Formulation		First Order Implicit

Table 3
Solution control criteria and absolute convergence criteria.

Solution control		Absolute convergence criteria	
density	1	x-velocity	10^{-5}
Body Forces	1	y-velocity	10^{-5}
pressure	0.3	energy equation	10^{-8}
momentum	0.7	continuity equation	10^{-5}
energy	0.8		
liquid fraction	0.9		

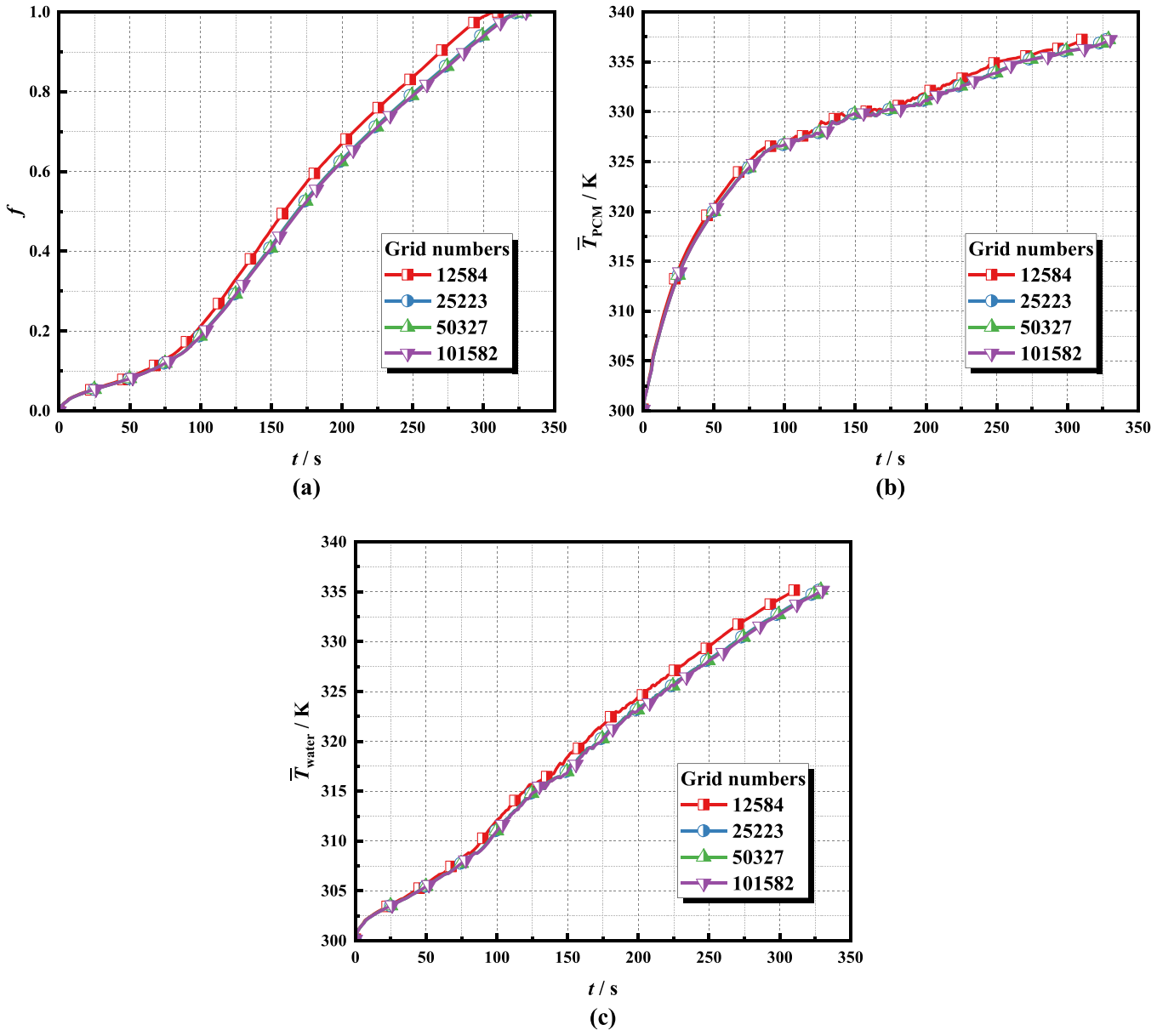

Fig. 4. The effect of different grid numbers: (a) liquidus ratio; (b) PCM mean temperature; (c) water mean temperature.

the ellipses decrease, the influence of wall temperature on melting velocity becomes more pronounced. Additionally, the melting time exhibited a positive correlation with the temperature distribution coefficient. Hirata et al [19] conducted experimental investigations into the melting characteristics of PCMs in horizontal rectangular capsules. They compared the effects of different aspect ratios and two types of PCM, applying the Nusselt liquid film theory to analyze the heat associated with phase transformation. The results indicated that, at larger Stefan numbers, the natural convection at 4 °C was more pronounced than that observed during ice melting.

Zhao et al [20] employed an enhanced Nusselt boundary layer model to characterize the heat charging process and developed a two-dimensional visualization experiment. Utilizing digital image processing, they recorded the distribution and rate of the liquid phase across seven rectangular cavities with varying oblique angles. The findings indicated that the dimensionless liquid fraction and height of PCM were in agreement with theoretical predictions, and the optimal melting time was achieved with a tilt angle of 60° Boroojerdian et al [21] utilized a non-contact measurement approach to directly quantify the liquid phase fraction during the contact melting of PCMs and conducted numerical investigations using a multiphase method. Their results demonstrated that the dimensions of solid PCM at different time intervals aligned with the calculations derived from the numerical model. Notably, when the solid fraction was low, the degree of solid subsidence was found to be less than the predicted numerical outcomes. Building on this theoretical framework, Hu and Fan [22] predicted changes in melt film thickness and the motion of unmolten solids within Kahlo and power-law fluids. They established a force balance relationship and corresponding numerical methods employing lubrication approximations. Experimental observations revealed a strong correlation between the experimental results and the numerical solutions for Carreau liquids. Consequently, they formulated a power-law model alongside an approximate analytical model for Carreau fluids. Further validation confirmed that the approximate solution is a convenient and efficient method for calculating the dynamic TES process of shear-thinning fluids.

With advances in computational fluid mechanics, commonly utilized models for the numerical simulation of charging processes encompass

mean temperature.

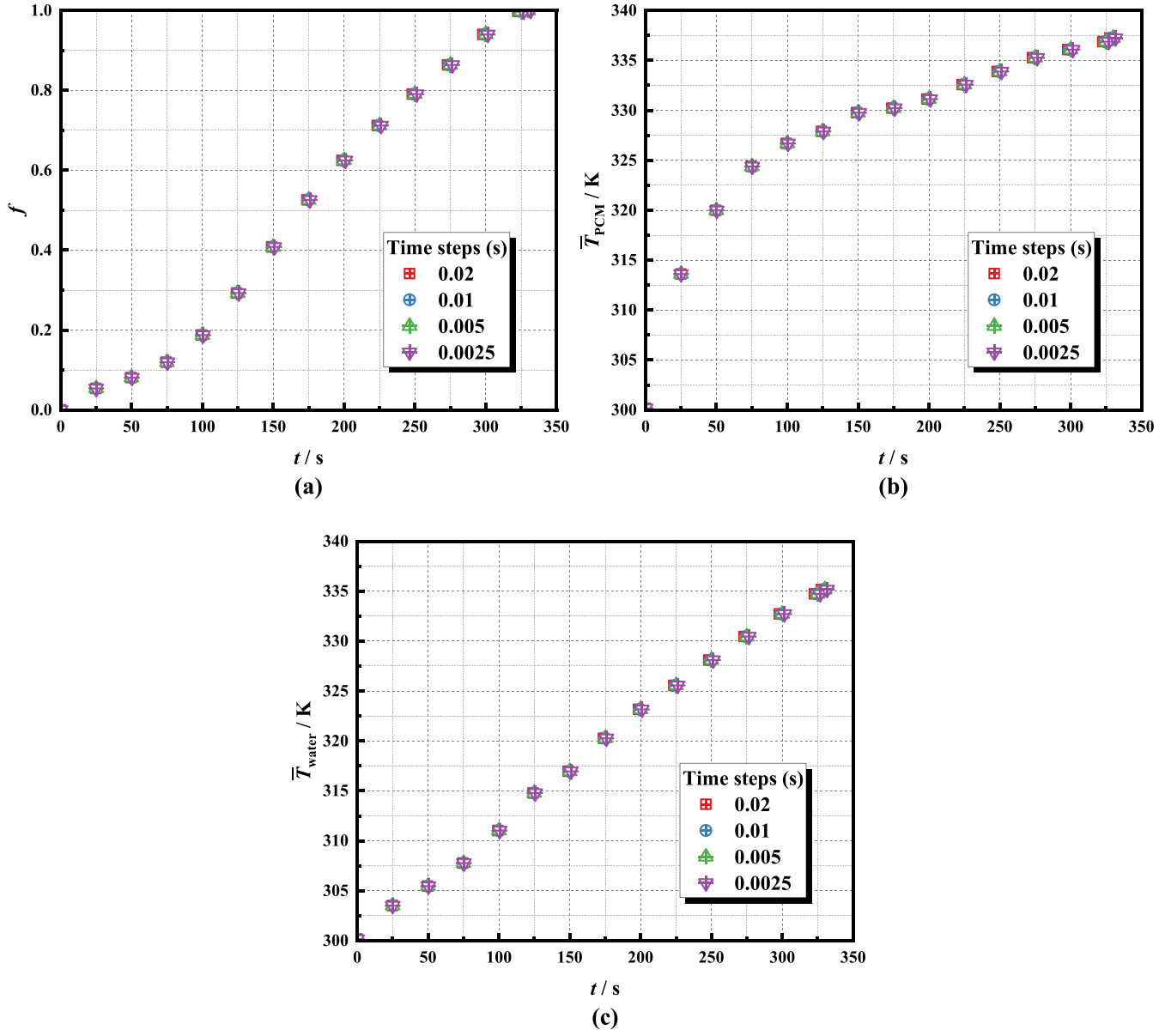

Fig. 5. The effect of different time steps: (a) liquidus ratio; (b) PCM mean temperature; (c) water mean temperature.

the heat conduction equation, the momentum equation, and the phase transition model [23,24]. By resolving these equations, it is possible to simulate the evolution of the melting zone, the changes of the melting rate and at the solid-liquid interface [25]. Key modeling methodologies include the enthalpy porous media model, the Volume of Fluid (VOF) model, and the Lattice Boltzmann method. Assis et al [26] performed numerical simulations of spherical phase-change energy storage units of varying diameters, investigating the contact melting phenomena induced by liquid phase convection, sinking of solid PCM, and volumetric expansion using Fluent software. Their study verified the numerical results through visual experiments, demonstrating that the geometric and thermal parameters of the system influence the transient phase transition process. Dimensional analysis indicated that the liquid phase rate correlates effectively with the mean Nusselt number, Stefan number, Grashof number, and Fourier number. Hosseinizadeh et al [27] employed both the enthalpy-pore model and the VOF model to conduct a transient numerical analysis of unconfined melting in a spherical vessel, while also preparing nano-composite phase change materials containing copper nanoparticles. By comparing three distinct Stefan numbers along with varying nanoparticle percentages, their findings revealed that increased thermal conductivity significantly enhanced the development of unconfined melting, thereby accelerating the melting velocity.

Kozak and Ziskind [28] developed a User-Defined Function (UDF) based on the enthalpy method within a fixed grid model to ensure that a solid body behaves as a rigid entity without undergoing stretching or deformation. The numerical model was validated against reference results, and the numerical outcomes were enhanced through dimensional analysis. The findings demonstrated that the model effectively addresses the complex melting problems associated with solid volume inertia and can model the complete rotation of solids and the expansion of melts within a specified temperature range. Ezra and Kozak [29] proposed a novel model for isothermal heating surfaces, enabling the derivation of analytical expressions for dimensionless melt thickness and the liquid phase rate of PCMs over time. Subsequently, a new approximate model

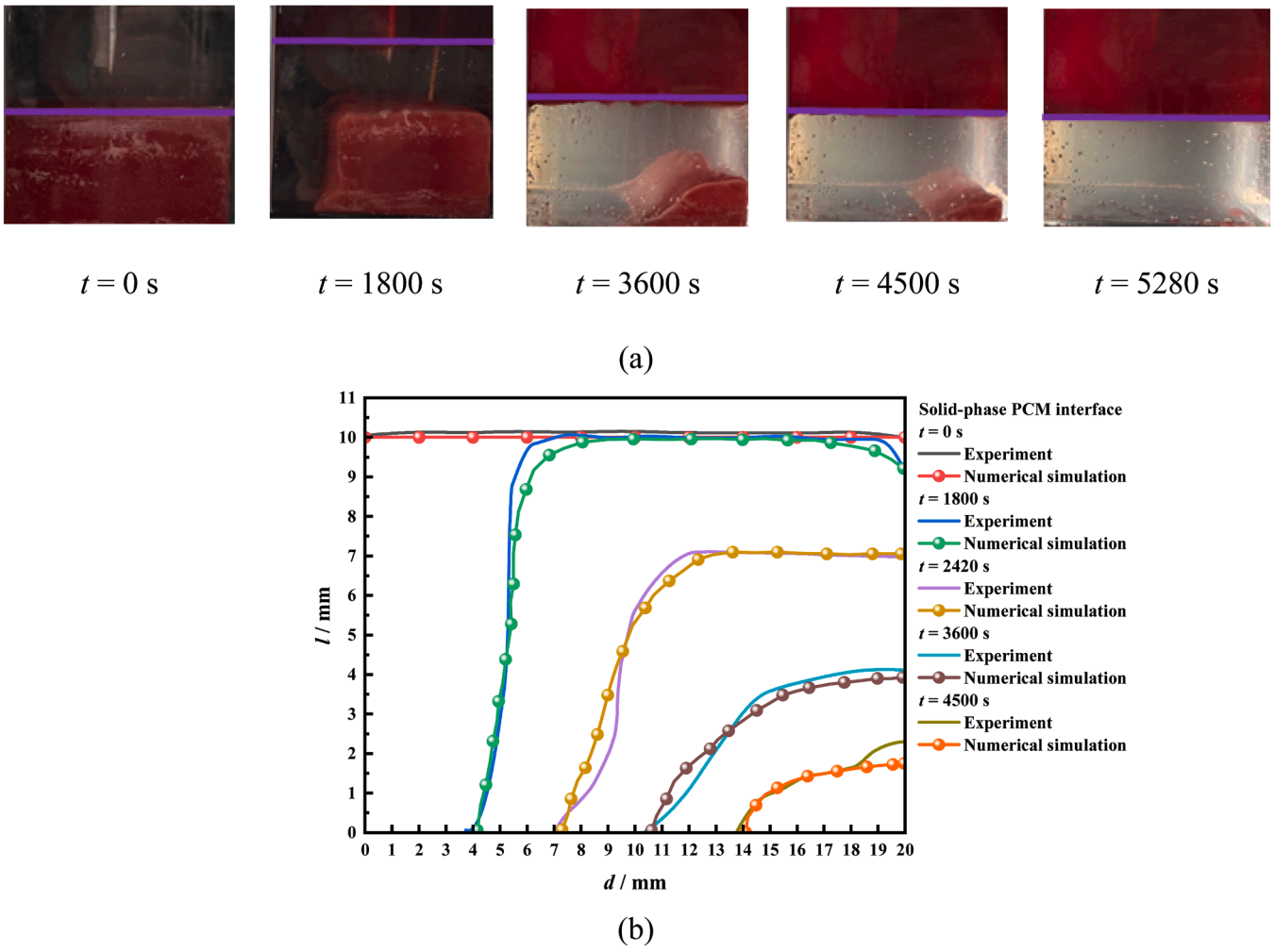

Fig. 6. (a) The evolution of the solid-liquid interface in the experiment at different times; (b) Comparison of the experimental and simulated solid-state PCM interfaces.

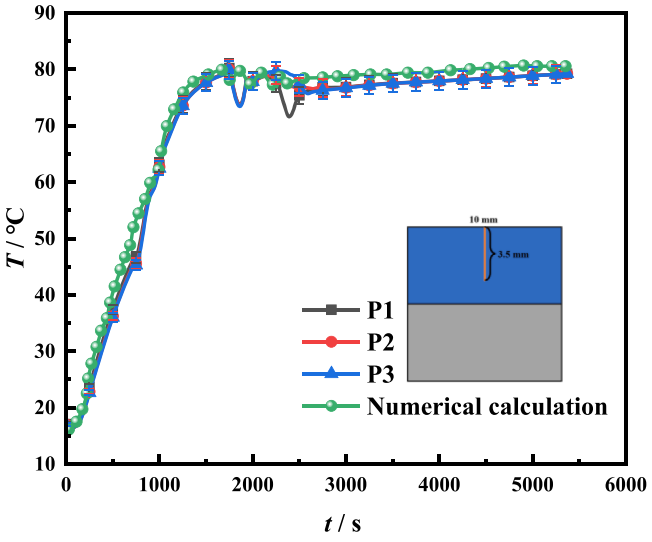

Fig. 7. Comparison of experimental temperature point measurements with numerical model.

was developed, and its predictions were rigorously compared with exact solutions and existing approximate methods. They derived a numerical model for heat convection under constant heat flux, elucidating the effect of external forces on the near-contact melting process. With an enhanced understanding of contact melting in phase-change TES systems, there has been considerable research aimed at improving heat transfer through the melting process. This work is primarily categorized into two approaches: increasing the number of contact melting zones and further minimizing the thermal resistance within these zones. The expansion of contact melting areas is primarily achieved by utilizing metal fins [30,31], while the reduction of thermal resistance can be accomplished through techniques such as machined grooves [32,33], incorporating porous particles [34,35], and employing nano-strengthening methods [36,37]. However, the prevailing strategy of enhancing the contact melting area through the use of large metal fins poses challenges, including difficulties in processing and potential negative impacts on heat storage. Additionally, metal fins may create localized high-stress areas within the container, which can inhibit the effectiveness of the increased contact melting area.

Building on the previous research focused on enhancing heat transfer through contact melting zones using water [38,39], this study introduced two distinct contact melting structures. In addition to a composite latent heat storage structure with water at the base to enhance heat transfer, a novel contact melting configuration was proposed, featuring 50 % solid PCM at the bottom and water at the top. Both structures were subject to numerical simulation and comparison. The distributions of the liquid phase, temperature, and internal flow velocity were analyzed throughout the heat transfer process across different contact melting conditions, allowing for a quantitative evaluation of the melting

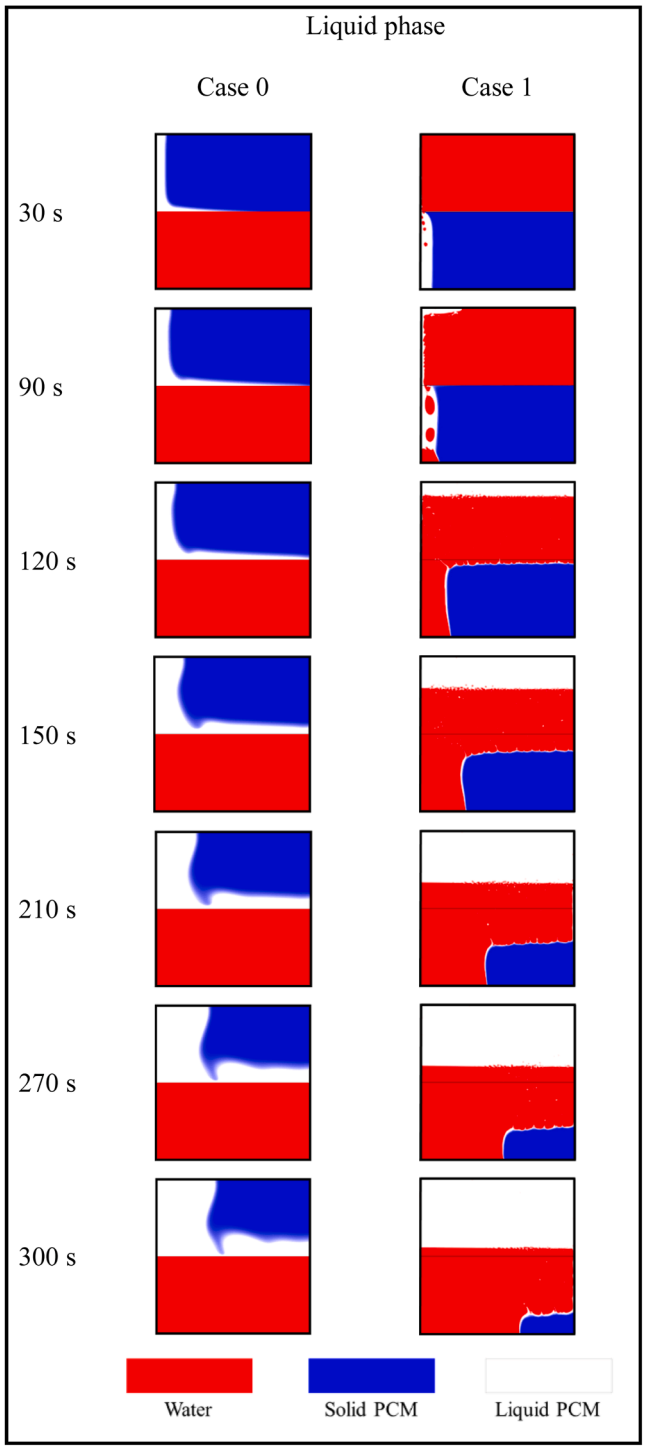

Fig. 8. Comparison of liquid phase of melting process between Case 0 and Case 1 (Vof model).

performance and energy storage capabilities. Furthermore, the melting properties of the novel contact melting structures were examined under varying wall temperatures.

2. Problem description

2.1. Physical model

As shown in Fig. 1, it is a comparison of the comprehensive energy utilization of traditional fossil fuel energy and renewable energy. By using phase change energy storage technology to recover waste heat, the economic efficiency and safety of energy can be effectively improved, which is of great significance for the heat utilization in industrial parks.

As shown in Case 0 in Fig. 2, it is the constructed traditional composite melting process. 50 % of the sensible heat material (water) is placed at the bottom of the PCM, and heat conduction is conducted to the PCM through the high thermal conductivity of water. Water is used as an enhanced heat exchange medium and also as a heat storage medium for enhancement. Case 1 is a newly proposed composite melting structure with PCM at the bottom and water at the top. Under the action of the heat source, the melted PCM, due to its lower density than water, exchanges positions with water and conducts deep heat exchange through the mass transfer process. The occurrence of this process is interesting. This study conducted experiments and numerical analyses on this process. The adopted square phase change energy storage structure is 20 mm in length and 20 mm in width, and the selected material is copper. The thermal and physical properties of water and the PCM used are detailed in Table 1.

2.2. Mathematical model

2.2.1. Model assumption

The integration of the Volume of Fluid (VOF) method with a CFD model to analyze the melting process of water and paraffin within a square cavity represents a classical multi-phase flow problem. This approach encompasses the intricate interactions between fluid dynamics, heat transfer, and the phase transitions between solid and liquid states. The VOF method is a widely accepted technique for addressing the challenges associated with free interfaces in multiphase flow and is particularly effective for tracking the evolution of fluid interfaces [38, 44]. The following assumptions underpin the governing equations for the subsequent analysis:

(1) Liquid PCM was represented as unsteady and incompressible laminar flow.
(2) Natural convection that occurs between the PCM and water was described by the Boussinesq approximation.
(3) The wall surface has a no-slip boundary, and viscous dissipation was ignored.
(4) Variations in volume during the solid-liquid phase transition were excluded from the analysis.
(5) Radiation heat transfer and heat loss from the external environment were ignored.

These assumptions provide a foundational framework for the ensuing analysis.

2.2.2. Mathematical model of case 0 (water at the bottom)

For water [45,46]:

Continuity equation:

$$\frac{\partial u}{\partial x}+\frac{\partial v}{\partial x}=0 \tag{1}$$

Momentum equation:

$$\rho_w\left(\frac{\partial u}{\partial t}+\frac{\partial uu}{\partial x}+\frac{\partial uv}{\partial y}\right)=-\frac{\partial p}{\partial x}+\mu_w\left(\frac{\partial^2 u}{\partial x^2}+\frac{\partial^2 u}{\partial y^2}\right) \tag{2}$$

$$\rho_w\left(\frac{\partial v}{\partial t}+\frac{\partial uv}{\partial x}+\frac{\partial vv}{\partial y}\right)=-\frac{\partial p}{\partial y}+\mu_w\left(\frac{\partial^2 v}{\partial x^2}+\frac{\partial^2 v}{\partial y^2}\right)+\rho_w\vec{g} \tag{3}$$

Energy equation:

$$\rho_w c_{p,w}\left(\frac{\partial T}{\partial t}+u\frac{\partial T}{\partial x}+v\frac{\partial T}{\partial y}\right)=k\left(\frac{\partial^2 T}{\partial x^2}+\frac{\partial^2 T}{\partial y^2}\right) \tag{4}$$

where u, v, ρ_w, μ_w, and $c_{p,w}$ separately represent x direction velocity, y

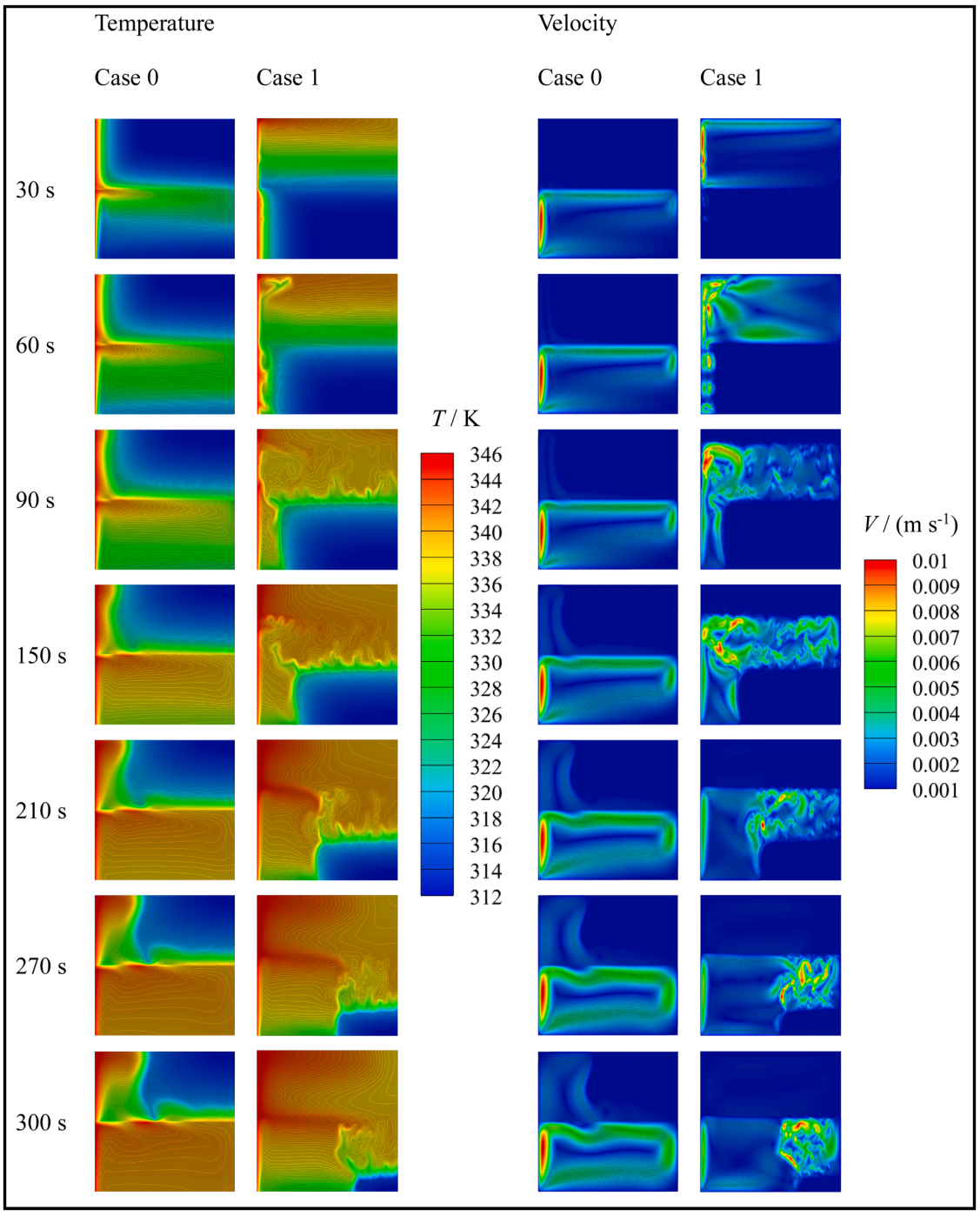

Fig. 9. Comparison of temperature and flow velocity of melting process between Case 0 and Case 1 (Vof model).

direction velocity, density, dynamic viscosity, and isobaric specific heat of water.

For PCM [47,48]:

Continuity equation:

$$\frac{\partial u}{\partial x}+\frac{\partial v}{\partial x}=0 \tag{5}$$

Momentum equation:

$$\rho_P\left(\frac{\partial u}{\partial t}+u\frac{\partial u}{\partial x}+u\frac{\partial v}{\partial y}\right)=-\frac{\partial p}{\partial x}+\mu_P\left(\frac{\partial^2 u}{\partial x^2}+\frac{\partial^2 u}{\partial y^2}\right)-A_{mush}\frac{(1-f)^2}{f^3+\varepsilon}u \tag{6}$$

$$\rho_P\left(\frac{\partial v}{\partial t}+u\frac{\partial v}{\partial x}+v\frac{\partial v}{\partial y}\right)=-\frac{\partial p}{\partial y}+\mu_P\left(\frac{\partial^2 v}{\partial x^2}+\frac{\partial^2 v}{\partial y^2}\right)-A_{mush}\frac{(1-f)^2}{f^3+\varepsilon}v+\rho_0 g\beta(T-T_m) \tag{7}$$

Energy equation:

$$\rho_P\left(\frac{\partial H}{\partial t}+u\frac{\partial H}{\partial x}+v\frac{\partial H}{\partial y}\right)=k_P\left(\frac{\partial^2 T}{\partial x^2}+\frac{\partial^2 T}{\partial y^2}\right) \tag{8}$$

where ρ_P, μ_P, p, β and T_m represent density of PCM, dynamic viscosity of PCM, pressure, thermal expansion coefficient, and melting temperature, respectively. The paste region constant (A_{mush}) reflects the osmotic resistance of solid-liquid interaction, is usually between 10^5–10^8 kg/m^3

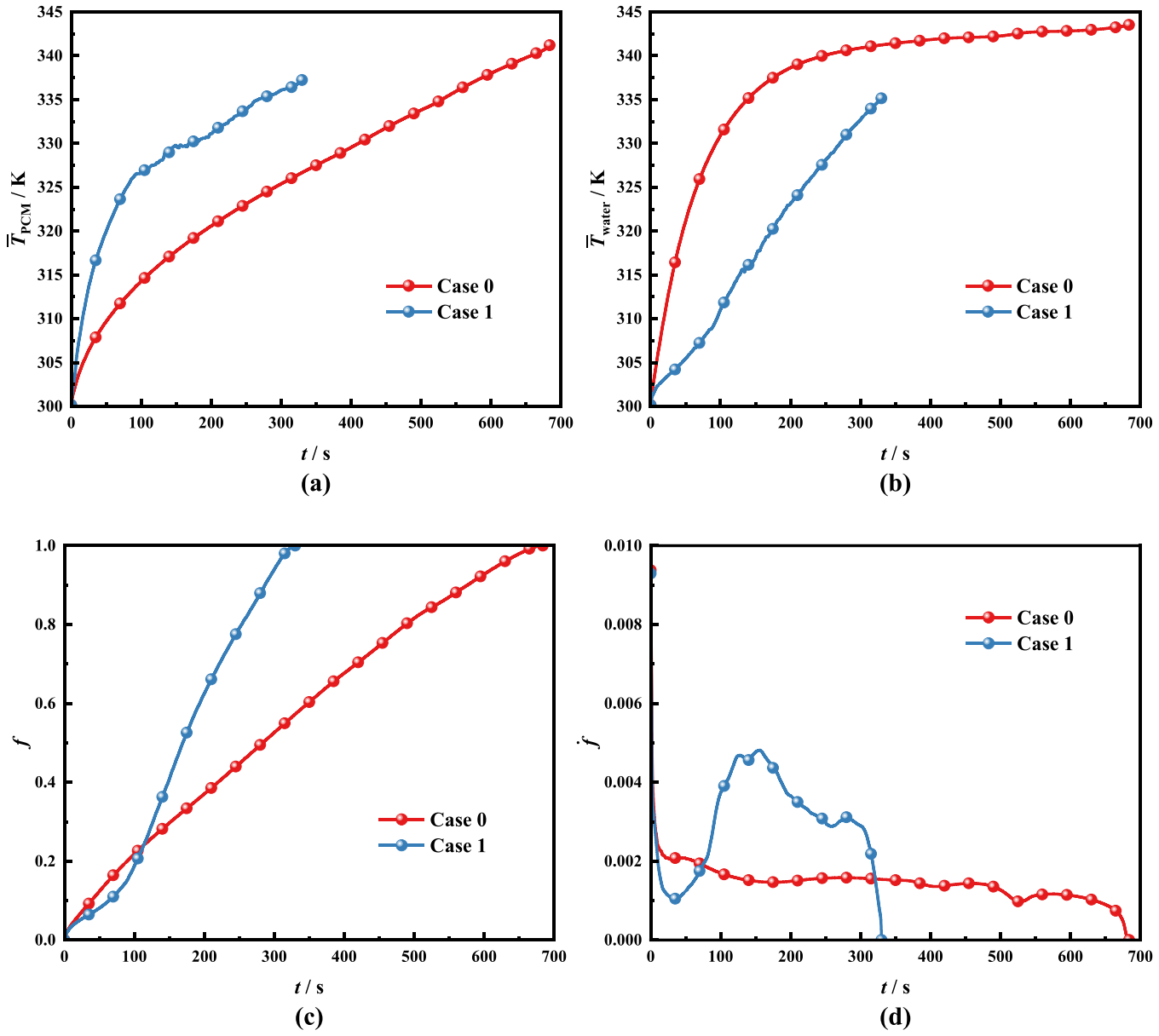

Fig. 10. Comparison of melting process between Case 0 and Case 1: (a) PCM mean temperature; (b) mean water temperature; (c) liquidus ratio; (d) heat charging rate.

s, to specify the momentum sink term in mushy region, and 10^6 kg/m^3 s here [49]. f was the liquid fraction, and $\dot{f}$ was melting rate [50]:

$$f = \begin{cases} 0, T \le T_s \\ \dfrac{T - T_s}{T_l - T_s}, T_s < T < T_l \\ 1, T \ge T_l \end{cases} \tag{9}$$

$$\dot{f} = \begin{cases} \dfrac{\partial f}{\partial t}, T_s < T < T_l \\ 0, T \le T, T \ge T_l \end{cases} \tag{10}$$

H signifies the total enthalpy of PCM:

$$H = h_{ref} + \int_{T_{ref}}^{T} c_p dT + f\lambda \tag{11}$$

2.2.3. Mathematical model of case 1 (PCM at the bottom)

The core of the VOF method was to track the volume fraction of each fluid phase to ensure the correct modeling of the phase interface. The mass conservation equation for each fluid phase in two dimensions was expressed as follows [49]:

$$\frac{\partial \alpha}{\partial t} + \nabla \cdot (\alpha \vec{u}) = 0 \tag{12}$$

where $\vec{u}$ denotes the flow rate, a determines the volume fraction, $a = 1$ represents a complete liquid phase, and $a = 0$ signifies a complete solid state. During a phase transition, a has a value between 0 and 1, indicating the location of the liquid-solid phase interface.

Momentum equation [51,52]:

water $$\rho_w \left(\frac{\partial \vec{u}_w}{\partial t} + \vec{u}_w \cdot \nabla \vec{u}_w \right) = -\nabla p + \nabla \cdot \mu_w \left(\nabla \vec{u}_w \right) + \rho_w \vec{g} \tag{13}$$

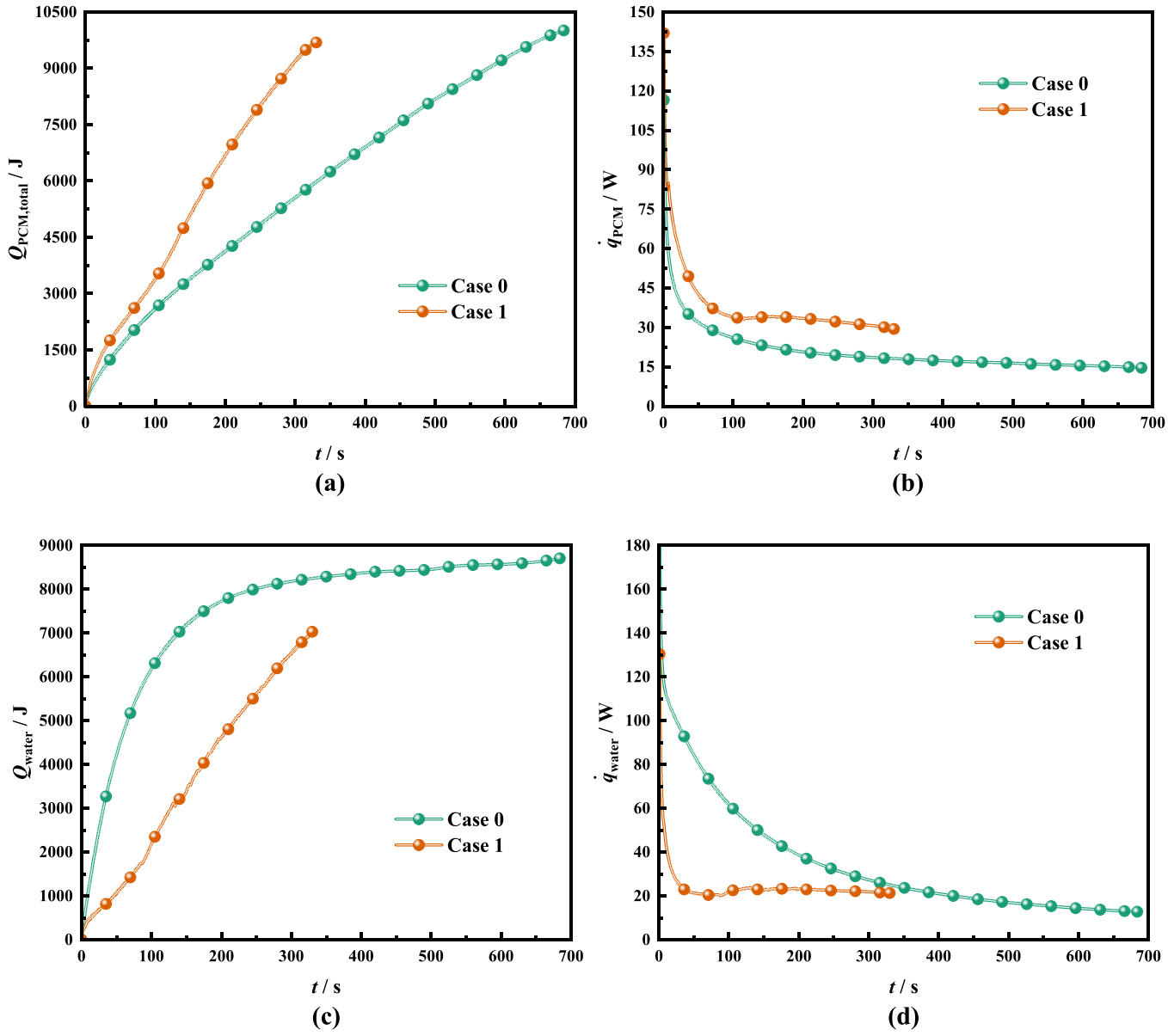

Fig. 11. Comparison of heat storage changes between Case 0 and Case 1: (a) PCM's energy storage; (b) PCM's energy storage rate; (c) water's energy storage; (d) water's energy storage rate.

PCM

$$\rho_p\left(\frac{\partial \vec{u}_p}{\partial t}+\vec{u}_p\cdot\nabla\vec{u}_p\right)=-\nabla p+\nabla\cdot\mu_p\left(\nabla\vec{u}_p\right)-A_{mush}\frac{(1-f)^2}{f^3+\varepsilon}u \tag{14}$$

$$\rho_p\left(\frac{\partial \vec{u}_p}{\partial t}+\vec{u}_p\cdot\nabla\vec{u}_p\right)=-\nabla p+\nabla\cdot\mu_p\left(\nabla\vec{u}_p\right)-A_{mush}\frac{(1-f)^2}{f^3+\varepsilon}v+\rho_0 g\beta(T-T_m) \tag{15}$$

where μ_w and μ_p indicate the dynamic viscosity of water and paraffin respectively, and $\vec{g}$ is the acceleration of gravity. The paste region constant (A_{mush}) is 10^6 kg/m^3 s here [49]. The Darcy damping factor is used to consider natural convection [53].

Energy equation:

$$\rho C_p\left(\frac{\partial T}{\partial t}+\vec{u}\cdot\nabla T\right)=-\nabla\cdot(k\nabla T)+\rho L\frac{\partial f}{\partial t} \tag{16}$$

Therefore, the total energy charging in PCM was shown below [54]:

$$Q_{total,\mathrm{PCM}}=m_{\mathrm{PCM}}\left[c_{p,\mathrm{PCM}}\left(T_{c,\mathrm{PCM}}-T_{i,\mathrm{PCM}}\right)+\lambda f\right] \tag{17}$$

Then the total energy charging of PCM-water was as follows:

$$Q_{total}=m_{\mathrm{PCM}}\left[c_{p,\mathrm{PCM}}\left(T_{c,\mathrm{PCM}}-T_{i,\mathrm{PCM}}\right)+\lambda f\right]+m_{\mathrm{water}}c_{p,\mathrm{water}}\left(T_{c,\mathrm{water}}-T_{i,\mathrm{water}}\right) \tag{18}$$

The instantaneous and average heat storage rate ($\dot{q}$, $\overline{q}$) were:

$$\dot{q}=\frac{\partial Q_{total}}{\partial t} \tag{19}$$

$$\overline{q}=\frac{Q_m}{t_m} \tag{20}$$

where Q_m and t_m were the total heat absorbed by the heat storage

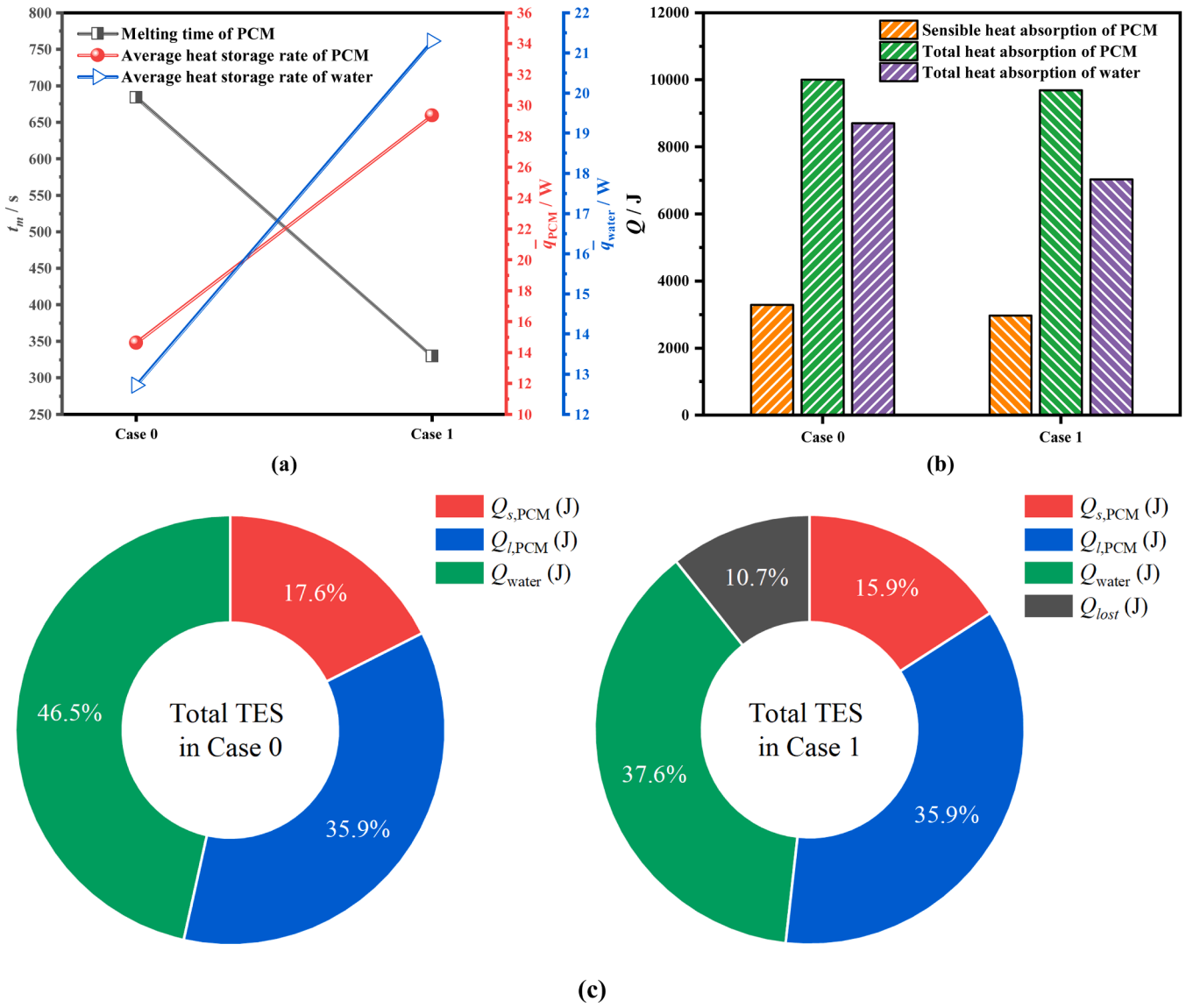

Fig. 12. Quantitative comparison between Case 0 and Case 1 at the end of melting: (a) melting time and average heat storage rate; (b) heat storage in different media; (c) dimensionless energy change analysis based on Case 0.

medium at the end of melting and the total melting time, respectively.

2.3. Initial and boundary conditions

Initial condition:

$$t = 0, T_{PCM} = T_{water} = 300.15K \quad (21)$$

The specific boundary conditions of the heat storage process were as follows:

$$T = T_w = 348.15K \quad (22)$$

The remaining boundaries were no slip conditions:

$$u_w = 0, v_w = 0 \quad (23)$$

3. Numerical calculation and experimental analysis

3.1. Numerical model construction and correlation analysis

In this study, numerical calculations were performed using Fluent 2021 R1. For Case 1, grid discretization was conducted as illustrated in Fig. 3. The grid was generated using an unstructured triangular mesh, with refined grids employed around the heat source and heat transfer boundaries. The numerical processes utilized a transient calculation method based on a pressure solver. The multi-phase flow and melting processes were modeled using melting-solidification, Volume of Fluid (VOF), and energy models. The pertinent solution and differentiation methods are outlined in Table 2, while solution control criteria and absolute convergence criteria are presented in Table 3. In the initial configuration, the PCM volume fraction at the bottom was set to 1, with the volume fraction of water in the upper region also set to 1.

The numerical algorithm process is as follows:

(1) Initialization settings: geometric model and mesh construction, setting of initial conditions and boundary conditions;
(2) Transient solution: solution of continuity, momentum and energy equations, calculation of VOF phase fraction, calculation of liquid phase fraction;
(3) Convergence and time step control: residual control, setting of adaptive time step;
(4) Post-processing and output: variable monitoring and visual analysis.

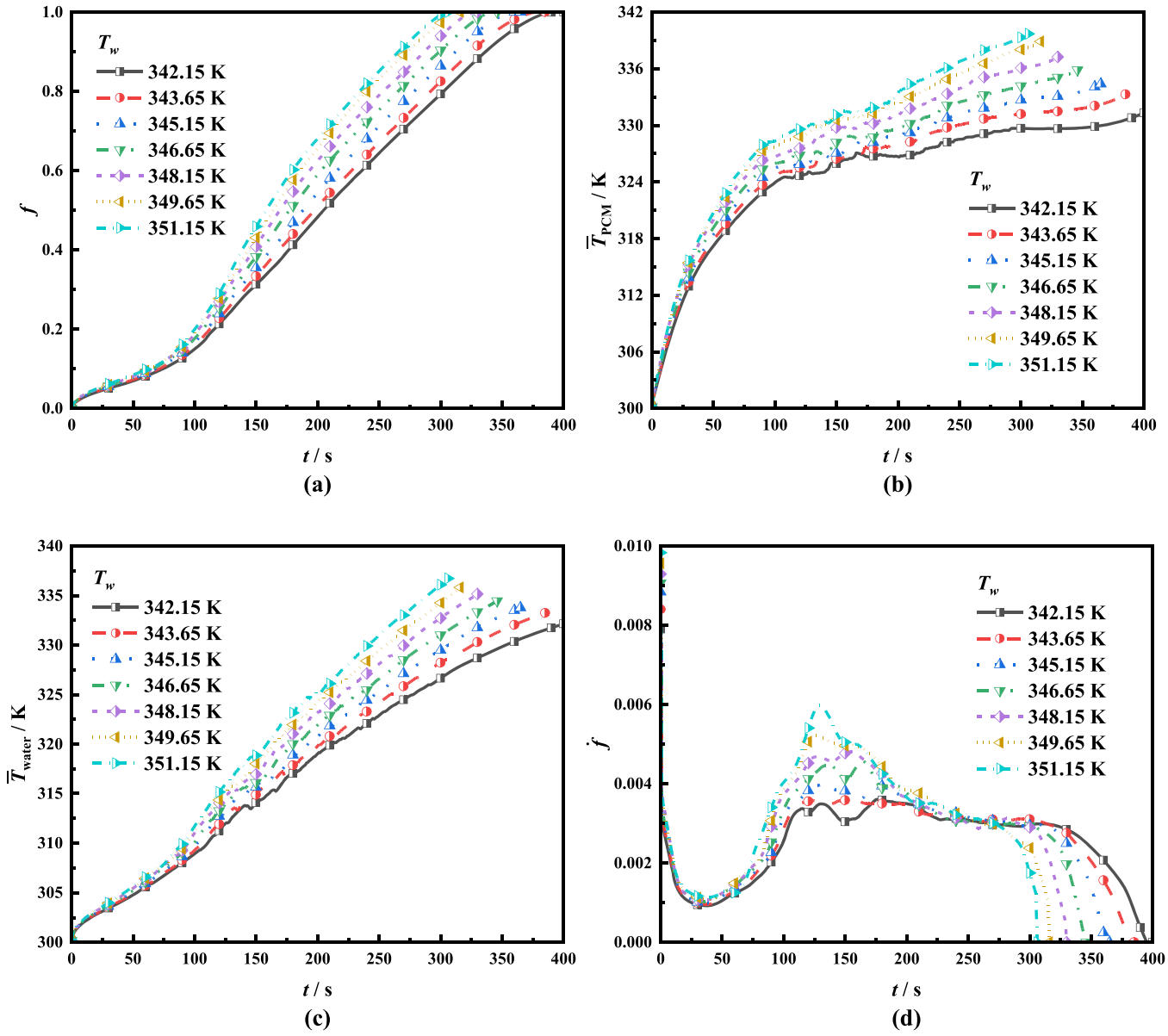

Fig. 13. Effect of different wall temperatures on melting process: (a) liquidus ratio; (b) average temperature of the PCM; (c) average temperature of the water; (d) melting rate.

Subsequently, an analysis was conducted for grid independence and time step selection for the numerical model in Case 1. Four grid configurations and four time-step intervals were chosen for comparison. The impact of varying grid numbers (12,584; 25,223; 50,327; and 101,582) on the liquid phase fraction of PCM, the average temperature of PCM, and the average temperature of water was presented in Fig. 4. Fig. 5 similarly depicts the influence of 0.02 s, 0.01 s, 0.005 s, and 0.0025 s time steps of PCM phase fraction, the average temperature of PCM, and the average temperature of water. The incorporation of the VOF model results in an increased computational time requirement. The findings show that, with a grid number exceeding 25,223 and a time step <0.01 s, the deviation in the numerical calculations for Case 1 remained below 2.47 %. When the time step is 0.01 s and the number of grids is 50,327, further reducing the time step or increasing the number of grids will only cause the numerical calculation deviation of the PCM liquid phase rate to be no >0.31 %. Therefore, subsequent calculations will use a time step of 0.01 s and a grid number of 50,327.

3.2. Experimental verification

Then, corresponding experiments were constructed to verify the VOF-CFD model. A square cavity heat storage unit with 50 % paraffin wax at the bottom and water at the top was established. The unit was a square cavity structure of 10 mm × 10 mm. The right side was heated at a constant temperature of 85 °C by a constant temperature electric heating system. Fig. 6 illustrates the evolution of the solid-liquid interface at various time points throughout the experiment, along with a comparative analysis of the solid PCM interface derived from both experimental and simulation data. Following the melting process at t = 1800 s and t = 3600 s, the paraffin wax exhibited continued ascent, culminating in the formation of a liquid PCM zone at the unit's apex. The comparative analysis reveals a congruence in the liquid paraffin heights, while minor discrepancies in the solid paraffin morphology at the base are observed, attributable to unavoidable experimental heat losses. Notably, the refractory zone positions are consistent. At the conclusion of the melting phase, 7.53 % deviation was noted between the experimental and simulated outcomes. Furthermore, thermocouples were

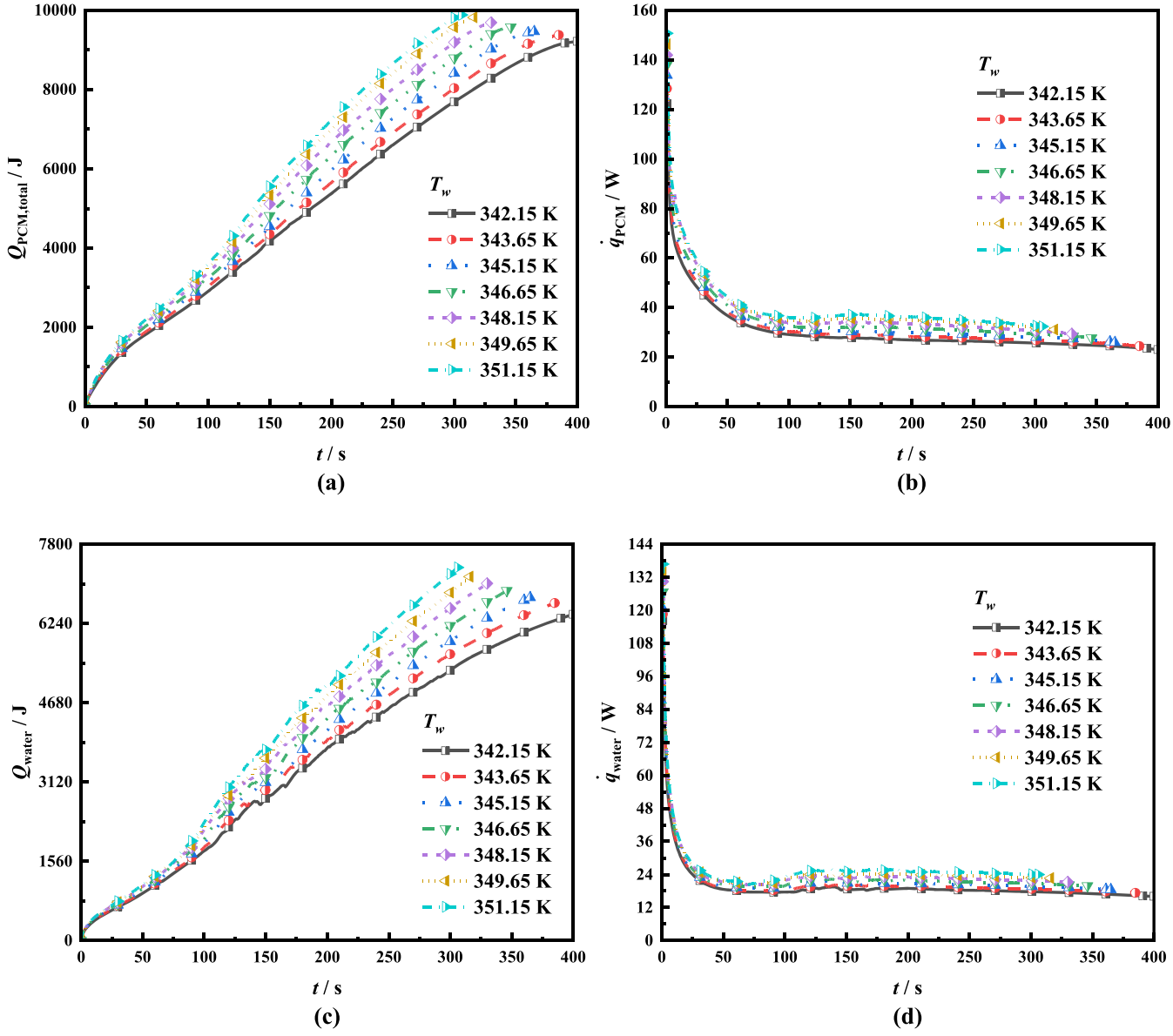

Fig. 14. Influence of different wall temperatures on energy storage process: (a) PCM's energy storage; (b) PCM's energy storage rate; (c) water's energy storage; (d) water's energy storage rate.

strategically positioned within the experimental apparatus for temperature assessment, as depicted in Fig. 7, specifically at a central location 3.5 mm from the upper section of the unit. These thermocouples were spaced at 3 mm intervals for temperature readings. Given the adoption of a two-dimensional analysis in the simulation, the simulated temperature measurement points were juxtaposed with the experimental thermocouple data (at the same level height), accounting for the measurement error inherent in the thermocouples. The comparative results, as presented in Fig. 7, indicate that the disparity between the experimental temperature measurement points and the numerical simulation data does not surpass 6.07 %, thereby validating the accuracy of the VOF-CFD model employed in this study.

4. Results and discussion

4.1. Novel heat charging process constructed by VOF model

This section presents a comparative analysis of the melting processes between Case 0, which features a composite phase-change TES structure with water at the bottom, and Case 1, which utilizes an innovative energy storage configuration with paraffin at the base. In Case 1, the model was constructed using the VOF method to detail the complex interactions between water and paraffin. Fig. 8 illustrates the evolution of liquid phase distribution over time for both Case 0 and Case 1.

The melting behaviors of Case 0 and Case 1 were analyzed independently. Initially, the heat source induced temperature increases in both the water and the paraffin wax. The paraffin wax on the left side commenced melting due to direct thermal contact with the heat source and the solid PCM. In Case 0, the presence of water in the lower half, which exhibits superior thermal conductivity compared to paraffin wax, facilitated the heating of the upper PCM through rapid heat absorption. At $t = 60$ s, the accelerated melting of the paraffin wax in the lower left region, assisted by the heated water, was evident. Driven by the combined effects of water and heat from the heat source, the heat storage process continued, and natural convection within the paraffin occurred. At $t = 210$ s, a solid refractory zone was observed in the lower right corner of the PCM. Ultimately, at the conclusion of the melting process, the low-temperature PCM was primarily concentrated in the region most

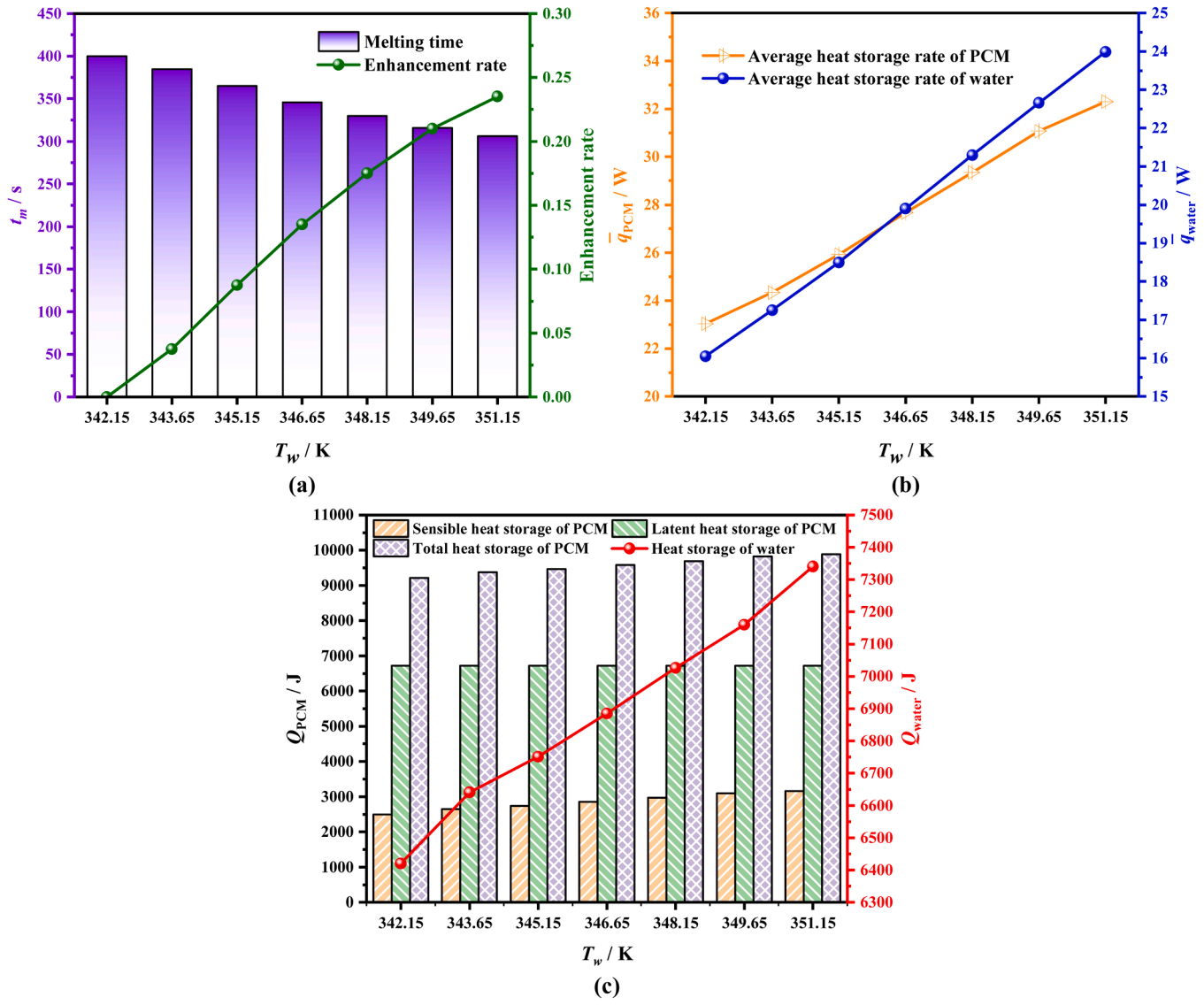

Fig. 15. Quantitative analysis of energy storage performance with different wall temperatures: (a) charging time; (b) mean rate of energy storage in different media; (c) heat storage in different media.

Table 4
RSM is used for parameter optimization in the heat storage process.

Model	Factor 1 A: Height of PCM (mm)	Factor 2 B: Heat source temperature (K)	Factor 3 C: Initial temperature (K)	Response 1 Comprehensive heat storage rate (W)	Response 2 Heat storage time (s)
1	8	345.15	300.15	48.12	316
2	12	345.15	300.15	32.89	536
3	8	351.15	300.15	59.72	275
4	12	351.15	300.15	43.18	431
5	8	348.15	296.15	56.26	304
6	12	348.15	296.15	38.74	495
7	8	348.15	304.15	51.74	284
8	12	348.15	304.15	37.05	461
9	10	345.15	296.15	46.02	377
10	10	351.15	296.15	57.75	319
11	10	345.15	304.15	42.91	352
12	10	351.15	304.15	52.63	319
13	10	348.15	300.15	50.64	331

distant from the heat source and water, specifically in the lower right section of the structure.

In Case 1, the initial configuration comprised a paraffin wax base layer. At $t = 30$ s, melting initiated in the paraffin adjacent to the walls due to the thermal input. As depicted in the two-phase distribution in the accompanying figure, the molten paraffin subsequently migrated towards the water-occupied region. By $t = 60$ s, a significant volume of melted paraffin was observed near the wall, with the liquid paraffin

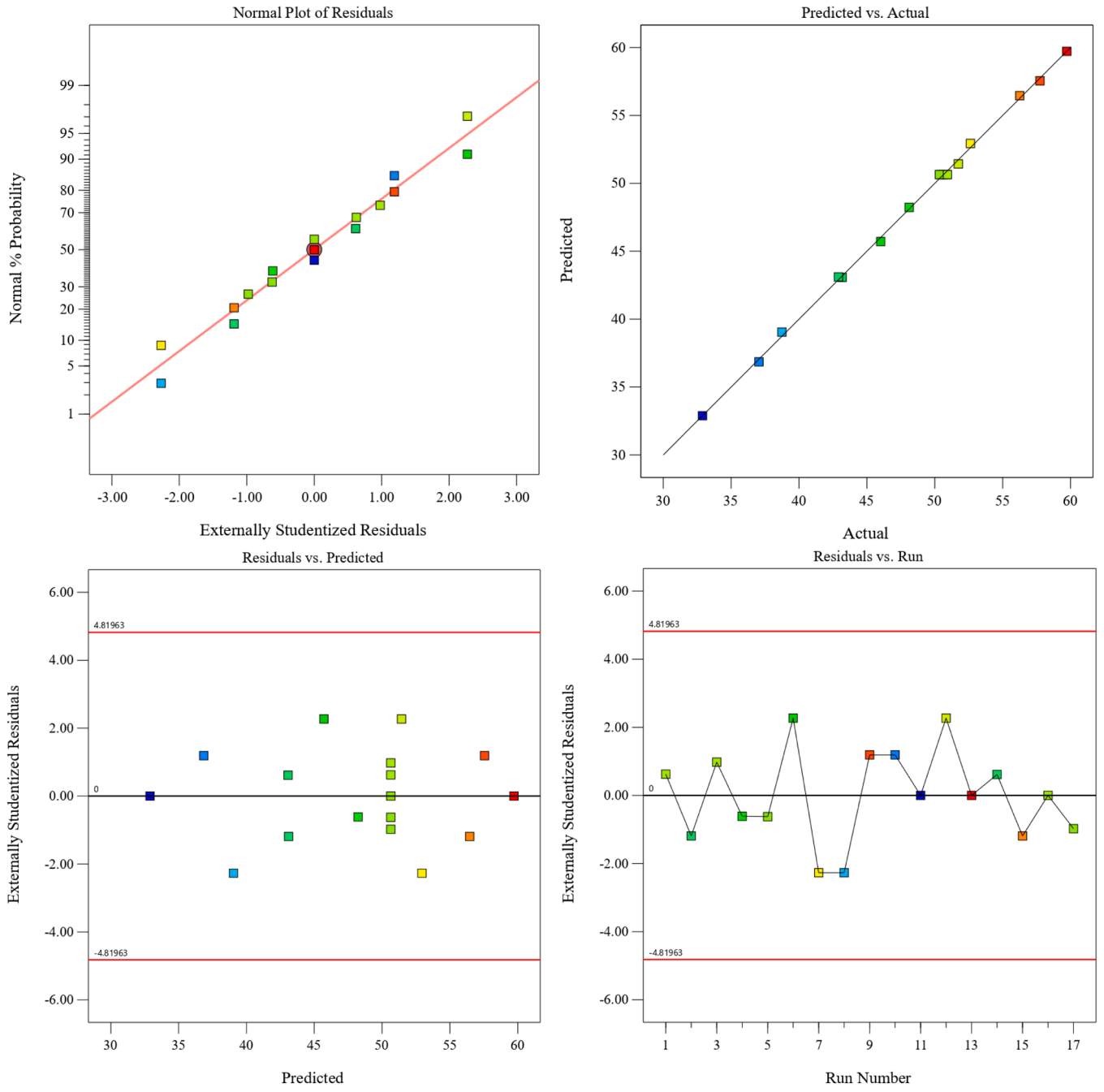

Fig. 16. (a) Normal distribution of residuals; (b) Predicted vs. Actual; (c) Residuals vs. Predicted; (d) Residuals vs. Run.

ascending to the upper left section of the structure, while some water descended. The continuous advection of both water and paraffin resulted in the formation of an irregular, non-planar interface. At $t = 90$ s, the paraffin in the lower left section of Case 1 exhibited accelerated melting, and the interfacial irregularity between the water and paraffin became more pronounced. The molten paraffin extended into the upper left of the model and continued to propagate horizontally towards the right, while the original solid paraffin region in the lower left was progressively displaced by descending water. By $t = 150$ s and 210 s, the liquid paraffin volume at the top of the model continued to expand, and the solid paraffin at the base steadily ascended due to melting. As the liquid paraffin level rose, it came into further contact with water, thereby enhancing the overall heat transfer performance. At the final stages of heat charging, it was clearly observed that in Case 1, only the lower right part of the solid paraffin had not melted. However, under the sustained thermal action of the encroaching water, the solid paraffin continued to exchange heat, enabling the melting rate to be maintained even during the final phase.

The changes in temperature distribution and flow velocity distribution subsequently in Case 0 and Case 1 were compared, as shown in Fig. 9. The temperature distribution reveals that, in Case 0, the increase in water temperature occurred more rapidly than that of paraffin wax. However, as water served as a secondary heat source for the paraffin after it had heated up, its subsequent temperature rise became inhibited. During the heating process, the internal flow rate of water remained consistently high, while the flow rate of paraffin became more and more intense during the mid to late stages of melting.

Based on the observed changes in temperature and flow rate in Case 1, at $t = 30$ s, the water temperature in the upper region rose rapidly, while paraffin near the wall in the lower section began to melt. At this

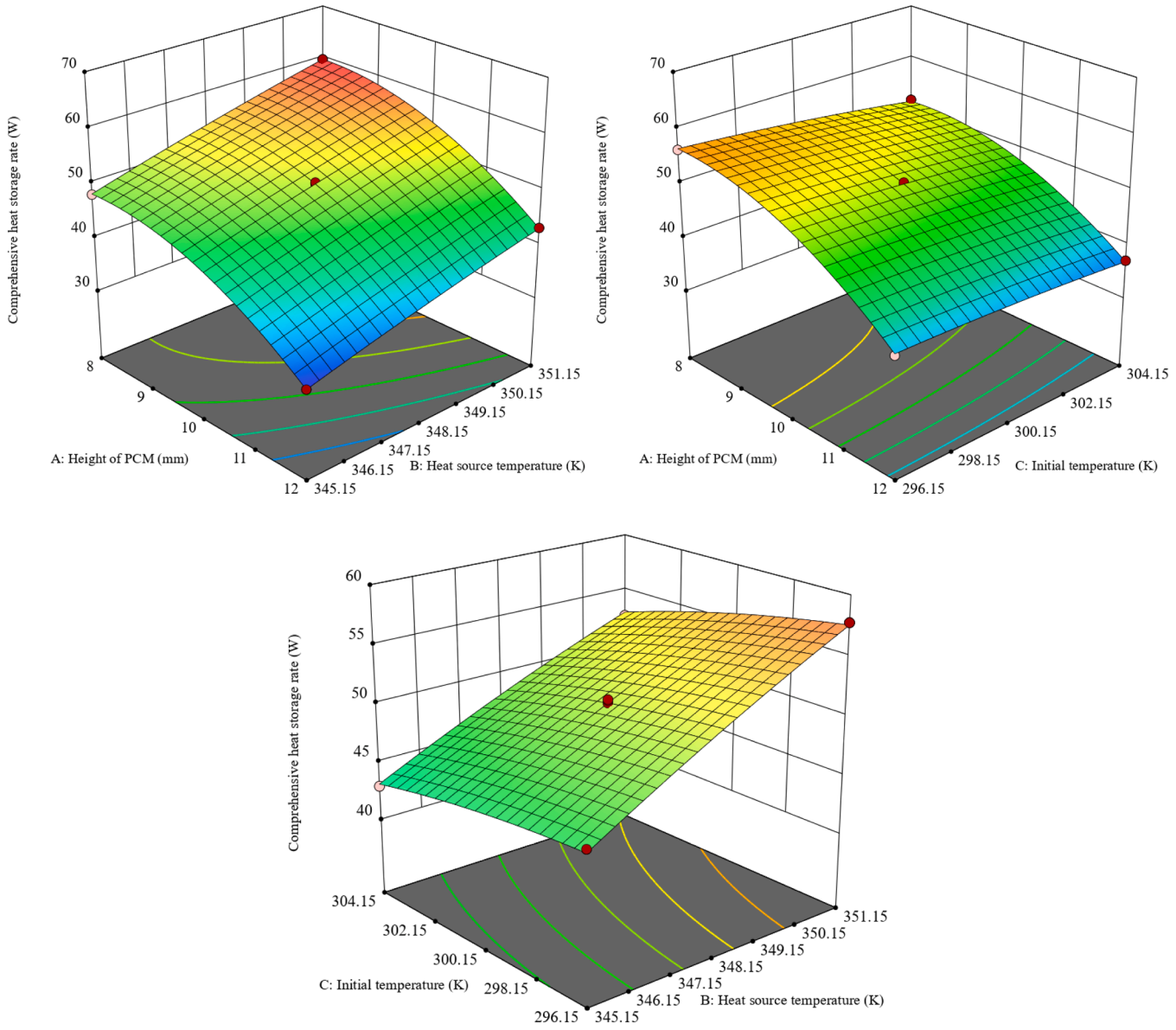

Fig. 17. Regarding the three-dimensional interaction of response 1.

stage, the internal flow rate of the upper water was significantly greater, and there was a minimal upward flow trend in the lower paraffin. By $t =$ 60 s, the lower paraffin continued its melting process and subsequent ascent due to density differentials, while the overlying water descended to occupy the vacated space. This descending, higher-temperature water contributed to the thermal loading of the paraffin on the right side. The resultant phase mixing attenuated the overall water flow rate, with high-velocity zones primarily localized at the water-paraffin interface. At $t =$ 90 s and 150 s, the internal water flow velocity in Case 1 became increasingly turbulent, as a substantial volume of molten paraffin ascended, displacing the upper water volume. Simultaneously, a significant region of lower-temperature paraffin was observed in the lower right quadrant. Conversely, the upper left region demonstrated elevated temperatures, attributable to its proximity to the heat source and convective heat transfer. As Case 1 approached its final thermal equilibrium at $t = 270$ s, molten paraffin occupied approximately 40 % of the upper section, establishing a distinct interface with the underlying water. The region below this interface maintained a higher temperature due to water's superior thermal conductivity. The remaining low-temperature paraffin continued to undergo thermal loading from the underlying water, resulting in further upward migration upon melting. At this juncture, the water phase near the heat source and its junction exhibited a high-velocity profile. This phenomenon intensified at $t =$ 300 s, and, upon completion of the melting process, Case 1 transitioned to a configuration comprising 50 % water at the bottom and 50 % paraffin at the top, thereby mirroring the characteristics of Case 0.

4.2. Quantitative comparison of melting properties of different contact melting processes

Based on the analysis of the melting processes in Case 0 and Case 1 presented in Section 4.1, this section delves deeper into the melting performance of both cases. A comparison of various parameters was provided as illustrated in Fig. 10. The rate of temperature rise of PCM in Case 1 significantly exceeded that of Case 0, with the most rapid increase observed during the pre-melting stage. In Case 1, the increase in water temperature was moderated by the heat exchange occurring between the descending water at the top of the unit and the ascending PCM, coupled with the necessity to heat the solid PCM. Conversely, the water temperature in Case 0 rose rapidly, experiencing a decline in the rate of

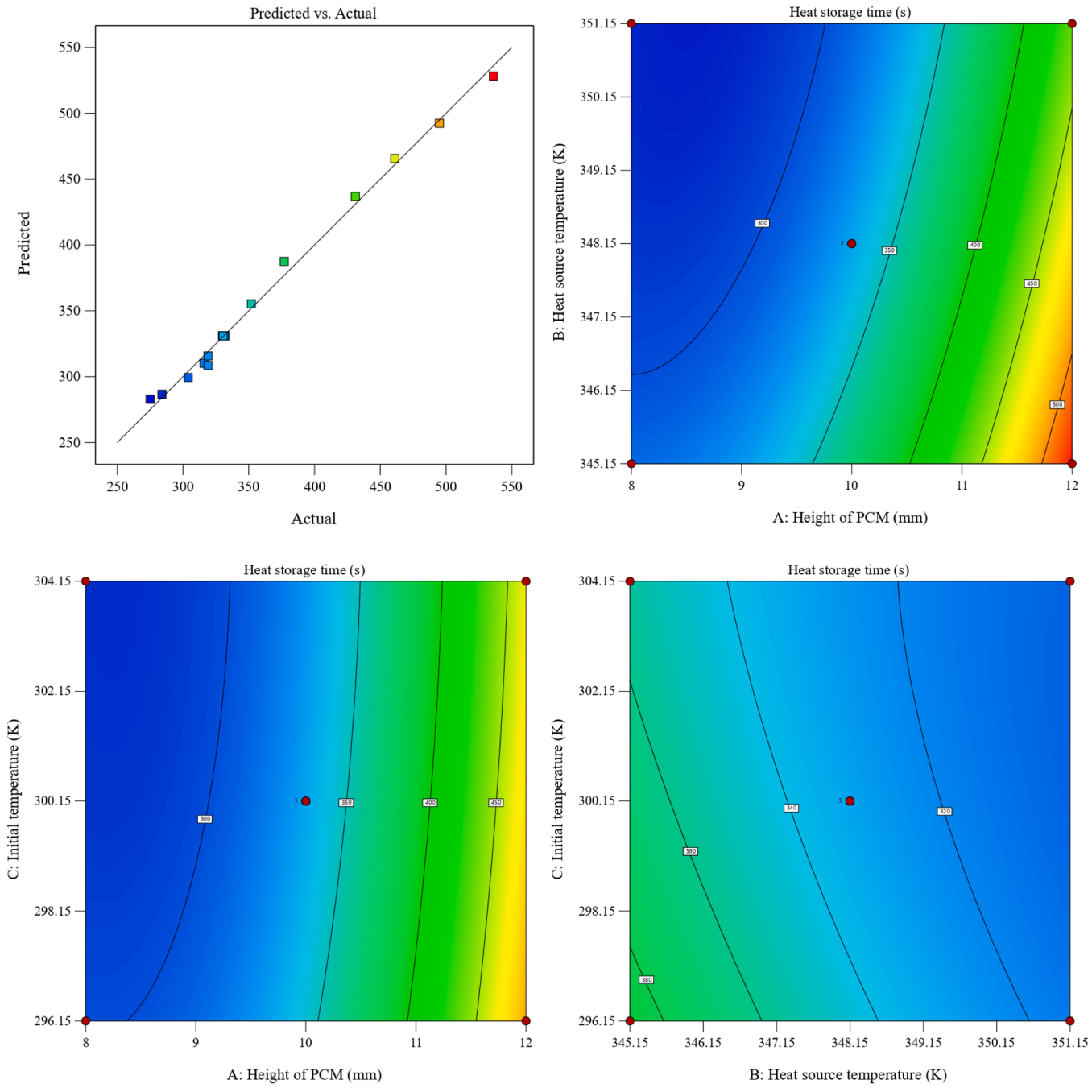

Fig. 18. RSM verification and two-dimensional interaction analysis of Response 2.

temperature increase only after 300 s due to a reduced temperature differential and diminished heat source. The examination of the liquid phase ratio of the PCM reveals that the initial growth of the liquid phase in Case 1 was relatively slow; this was attributed to the fact that the unit's heat was predominantly absorbed by the water at this stage, and the melted PCM heat was absorbed by water, resulting in a slow growth of the liquid phase rate of PCM. However, after 100 s, the liquid phase ratio experienced a rapid ascent, maintaining a steady rise. The water acted as a secondary heat source at the bottom in Case 0, thus improving the melting process at a consistent rate. Nonetheless, the enhanced contact melting performance of Case 1 facilitated a markedly superior heat transfer effect. When comparing the melting rates of the PCM, it is evident that in Case 1, the flows of paraffin and water resulted in noticeable fluctuations in the melting rate. Initially, the melting rate decreased continuously, followed by a rapid increase, before abruptly dropping to zero. In Case 1, the melting rate remained high in the heat charging stage, while in Case 0, the melting rate was very low in the middle and late stages. This analysis underscores that the internal flow characteristics of Case 1 significantly enhanced its melting rate compared to Case 0.

The heat absorption characteristics of Case 0 and Case 1 are compared in Fig. 11. The PCM in Case 1 exhibited significantly faster energy absorption compared to Case 0. Both cases demonstrated a peak in the instantaneous storage rate of PCM at the onset of charging, followed by a rapid decline that eventually stabilized. Notably, throughout the entire melting cycle, the instantaneous storage rate of PCM in Case 1 consistently surpassed that of Case 0. Regarding the heat absorption by water, the heat absorption rate in Case 0 was faster than in Case 1. In

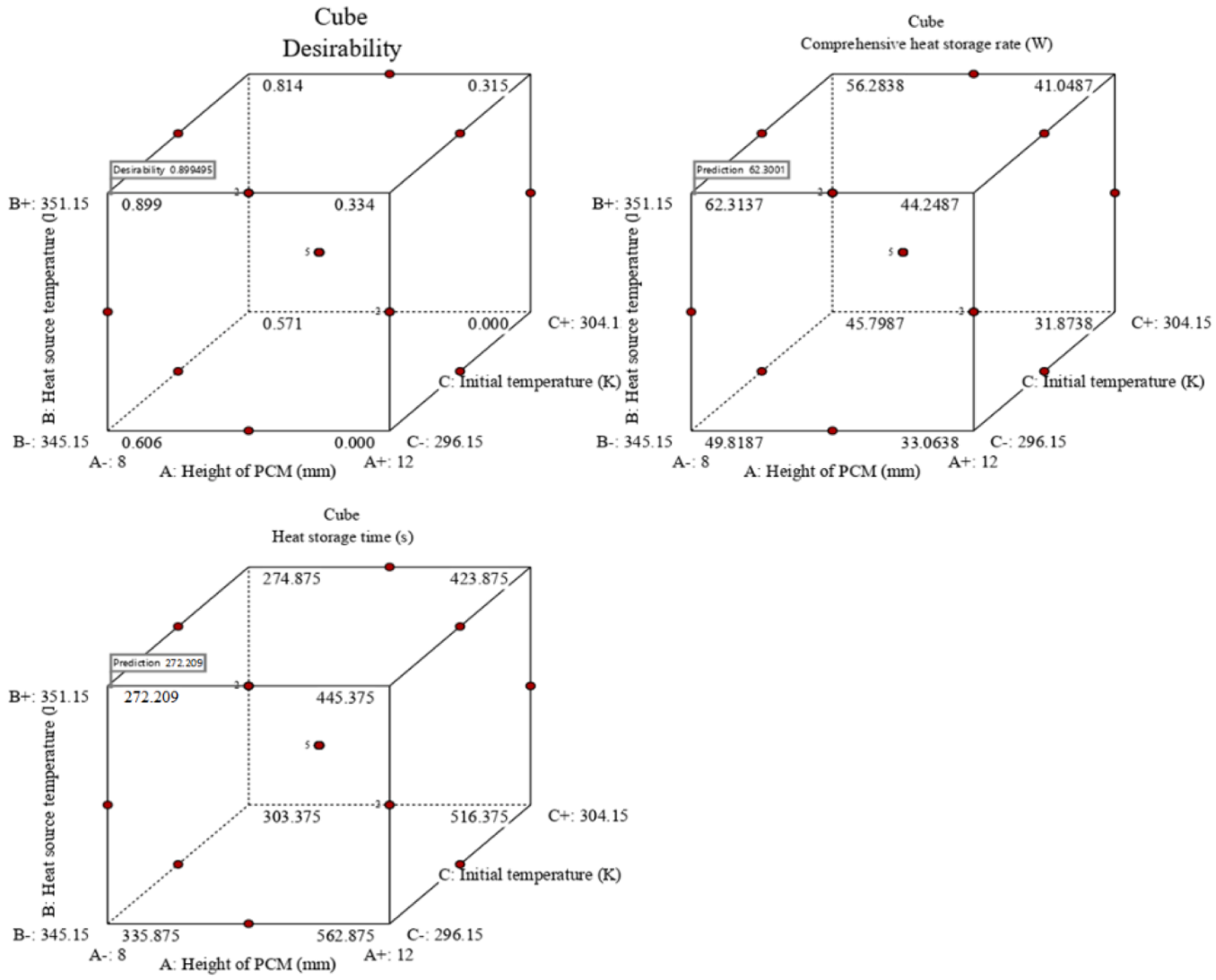

Fig. 19. The results of dual-objective optimization design.

Table 5
Analysis of dual-objective optimization results and actual errors.

Factor	Name	Level	Predicted value		Actual value	
			Response 1	Response 2	Response 1	Response 2
A	Height of PCM (mm)	8.05	62.3001	272.209	61.68	270.5
B	Heat source temperature (K)	351.15				
C	Initial temperature (K)	296.15				

Case 0, the water's heat absorption entered a slower phase during the middle and later stages of melting, leading to a loss of energy. Conversely, in Case 1, the water's instantaneous charging rate remained consistently lower than that in Case 0. Although a slight rebound followed an initial decline, the overall heat absorption rate remained low. Nevertheless, due to the longer melting duration of Case 0, the instantaneous heat absorption rate at the end of the charging process was lower compared to that of water in Case 1.

Fig. 12 presents a quantitative comparison between Case 0 and Case 1 at the conclusion of the heat charging process: (a) charging time and mean rate of energy storage; (b) energy storage in various media and (c) dimensionless energy change analysis based on Case 0. In Case 1, the melting time of PCM decreased by 51.75 % compared to Case 0. Furthermore, the average heat storage rate of the PCM and water increased by 101 % and 67 %, respectively, in Case 1 compared to Case 0. The higher average energy storage rate of water in Case 1 is due to the extended melting time in Case 0, which limits the overall heat transfer rate. Based on the analysis of dimensionless energy storage capacity, a comparison of heat storage across different media in Case 1 indicates that the total heat storage for PCM and water decreased by 3.2 % and 19 %, respectively, relative to Case 0. Consequently, the energy storage by PCM and water during the melting cycle in Case 1 was reduced by 10 % compared to Case 0. Therefore, while the novel contact melting model significantly reduced the heat charging time and improved the energy storage rates of both heat storage media compared to the traditional composite model with water at the bottom, it resulted in a decrease in overall energy storage.

4.3. Comparative study on the effect of heat source temperature on phase transformation process

This section analyzes the melting performance of the Case 1 structure under various heat source temperatures. Temperatures of 342.15 K, 343.65 K, 345.15 K, 346.65 K, 349.65 K, and 351.15 K were examined in addition to the original heat source temperature of 348.15 K. As depicted in Fig. 13, an analysis of the influence of varying heat source temperatures on the liquid phase ratio of PCM in the Case 1 structure reveals that increasing the heat source temperature can consistently enhance the internal melting rate of the energy storage unit. However, it has minimal impact on the early stages of the melting process. The evolution of the mean temperatures of the PCM and water indicates that the interaction between these two media causes fluctuating temperature increases, particularly evident in the average temperature of the PCM, which can even experience a decline. When the wall temperature rises, the temperature of the energy storage medium increases more rapidly, resulting in higher temperatures for both the PCM and water at the conclusion of the charging process. Furthermore, changes in the melting rate of PCM exhibit an initial rapid decrease, followed by an increase and a gradual decline thereafter. This rate fluctuates significantly in response to the different heat sources, with the heating effect at 351.15 K yielding the highest melting rate observed for the unit.

Fig. 14 illustrates the influence of varying heat source temperatures on the energy storage and energy storage rates of the unit. An increase in heat source temperature leads to a simultaneous rise in the heat storage by both PCM and water, with the total heat stored by these materials at the end of the corresponding charging process also exhibiting a consistent increase. Analyzing the changes in the PCM and water's instantaneous energy storage rates reveals that the initial energy storage rate was the highest, followed by a rapid decline to a more stable level. Nevertheless, a higher wall temperature resulted in an increased water's instantaneous energy storage rate. Consequently, both the PCM's heat storage rate per unit time and the water's instantaneous energy storage rate were enhanced.

Fig. 15 quantitatively analyzes the energy storage performance at different wall temperatures at the conclusion of the melting process. The analysis demonstrates that an increase in heat source temperature significantly enhanced the heat charging process of the novel energy storage structure in Case 1. Specifically, the melting time of the PCM was reduced by 18 % and 24 % at wall temperatures of 348.15 K and 351.15 K, respectively, compared to the condition at 342.15 K. Additionally, when compared to a wall temperature of 342.15 K, for both PCM and water the mean heat charging rates of at 348.15 K increased by 28 % and 33 %, respectively, while at 351.15 K, these rates rose by 40 % and 50 %, respectively. When examining the final energy storage, the wall temperature of 348.15 K resulted in increases of 5.1 % and 9.4 % in energy storage for PCM and water, respectively, compared to the data for a wall temperature of 342.15 K. Furthermore, at a wall temperature of 351.15 K, energy storage was 7.3 % higher than that at 342.15 K, with the heat storage of PCM and water increasing by 14 %.

4.4. Research on parameter optimization on phase transformation process

This section conducts an optimization study on different parameters of the Case 1 structure through the response surface method. The height of the bottom PCM, the temperature of the heat source, and the initial temperature of PCM-water were selected as variables. The design ranges were [8 mm, 12 mm], [345.15 K, 351.15 K], [296.15 K, 304.15 K], respectively. Taking the comprehensive heat storage rate (PCM+water) and the total heat storage time as the research variables, the calculation results of the Box-Behnken design were shown in Table 4.

In Fig. 16, the normal distribution of residuals for response 1, the predicted versus actual values, and the residuals versus predicted values were presented. The predicted values and the residual versus experimental comparison were graphed. The proximity of the residual data points to a straight line, along with the even distribution of predicted and actual values around the 45° line, suggests a strong correlation between the model's predicted and actual values. The random distribution of residuals, without temporal influence, indicated a sound experimental design, free from systematic error. Since the verification for response 2 is consistent with that of response 1, there is no need to elaborate further on this point.

As shown in Fig. 17, it was the analysis of the interaction of different parameters regarding response 1. As the height of PCM decreases and the temperature of the heat source increases, the comprehensive heat storage rate can be continuously enhanced. However, increasing the initial temperature of PCM and water can lead to a certain degree of reduction in the comprehensive heat storage rate. As shown in Fig. 17, it was the RSM verification and interaction analysis of response 2. Since the verification process was consistent with response 1, it has been simplified here. It can be known from Fig. 18(a) that the predicted values and the actual values were uniformly distributed around the 45° line. Moreover, based on the 2D interaction analysis, it can be known that with the increase of the initial PCM, the decrease of the heat source temperature and the increase of the initial temperature of the heat storage medium, the energy storage time will continuously increase.

This optimization process further presents the relationship between the design parameters and responses 1 and 2, as follows:

$$\text{Comprehensive heat storage rate} = -12450.92 + 9.81A + 45.19B + 29.05C - 0.055AB + 0.088AC - 0.042BC - 1.07A^2 - 0.043B^2 - 0.026C^2 \quad (24)$$

$$\text{Heat storage time} = 16552.6 + 849.34A - 690.77B - 315.43C - 2.67AB - 0.44AC + 0.52BC + 12.84A^2 + 0.79B^2 + 0.23C^2 \quad (25)$$

where based on the above relationship, further optimization analysis was conducted. The target of the comprehensive heat storage rate was set as the maximum and the target of the total heat storage time was set as the minimum. As shown in Fig. 19, it was a schematic diagram of the dual-objective optimization design. It can be seen that when Height of PCM = 8.05 mm, Heat source temperature = 351.15 K, and Initial temperature = 296.15 K, the objective function takes the optimal value. As shown in Table 5, the dual-objective optimization results and the actual error analysis were presented. At this point, the error between the predicted comprehensive heat storage rate and the actual value was 1.005 %, and the error between the predicted heat storage time and the actual value was 0.63 %. Moreover, the obtained actual values have a better optimization effect compared to other results. The optimization reliability of the RSM method has been proved.

5. Conclusions

This study analyzed two contact melting structures featuring water and solid PCM numerically. The validity of the numerical model is verified by experiments. The evolution of the liquid phase, temperature

distribution, and internal flow velocities for different contact melting configurations during the heat transfer process was compared, along with a quantitative assessment of melting and energy storage performance. Moreover, the melting characteristics of the novel contact melting structures under varying wall temperatures were further examined. The key findings are summarized as follows:

(1) In Case 1, where solid paraffin wax was situated at the bottom, the melted paraffin wax, influenced by the vertical wall temperature, rose into the water region and extended horizontally to the right. This movement caused a portion of the water to flow downwards, resulting in an irregular, jagged appearance of the original interface.
(2) The high temperature of the descending water during the melting process enabled the paraffin wax on the right side of Case 1 to contribute to the heating effect. This mixing reduced the overall flow velocity of the water, with elevated flow velocities primarily concentrated in the region where water and paraffin were actively interacting.
(3) In Case 1, the liquid phase rate initially increased slowly because the water predominantly absorbed the heat during this phase, while the melted PCM heat was absorbed by water. However, the subsequent melting rate for this structure remained consistently higher than that of Case 0, in which the water was positioned below the PCM, resulting in a shorter overall melting time.
(4) The melting time required for the PCM in Case 1 was reduced by 52 % compared to Case 0, while the mean velocities of the water and PCM increased by 67 % and 101 %, respectively, relative to Case 0. Nonetheless, the total heat storage of the PCM and water in Case 1 was lower by 3.2 % and 19 %, respectively, than in Case 0.
(5) The increase in wall temperature effectively enhanced both the internal melting rate and energy storage of the energy storage unit. Specifically, compared to a temperature of 342.15 K, the melting time of the PCM was reduced by 18 % and 24 % at wall temperatures of 348.15 K and 351.15 K, respectively. Additionally, at a wall temperature of 351.15 K, there was a 14 % increase in heat storage for both PCM and water, when compared with a wall temperature of 342.15 K.
(6) Design optimization of RSM based on Case 1, when height of PCM = 8.05 mm, heat source temperature = 351.15 K, and initial temperature = 296.15 K, the comprehensive heat storage rate and heat storage time were the optimal values, and the error between the predicted value and the actual value does not exceed 1.003 %.

CRediT authorship contribution statement

Xinyu Huang: Writing – review & editing, Writing – original draft, Validation, Software, Methodology, Formal analysis. **Yuan Xie:** Validation, Investigation, Data curation, Conceptualization. **Yuanji Li:** Visualization, Validation, Software, Investigation. **Haichuan Luo:** Writing – review & editing, Investigation, Formal analysis. **Jie Xue:** Visualization, Validation, Formal analysis. **Xiaohu Yang:** Writing – review & editing, Writing – original draft, Resources, Project administration, Methodology, Funding acquisition. **Hussam Jouhara:** Writing – review & editing, Writing – original draft, Validation, Investigation, Formal analysis, Conceptualization.

Declaration of competing interest

The authors declare that they have no known competing financial interests or personal relationships that could have appeared to influence the work reported in this paper.

Acknowledgments

This work was supported by the Key Scientific and Technological Innovation Team of Shaanxi Province (2023-CX-TD-29).

Data availability

No data was used for the research described in the article.

References

[1] E. Pomerantseva, F. Bonaccorso, X. Feng, Y. Cui, Y. Gogotsi, Energy storage: the future enabled by nanomaterials, Science 366 (2019) eaan8285.
[2] J.A. Dowling, K.Z. Rinaldi, T.H. Ruggles, S.J. Davis, M. Yuan, F. Tong, N.S. Lewis, K. Caldeira, Role of long-duration energy storage in variable renewable electricity systems, Joule 4 (2020) 1907–1928.
[3] N.A. Sepulveda, J.D. Jenkins, A. Edington, D.S. Mallapragada, R.K. Lester, The design space for long-duration energy storage in decarbonized power systems, Nat. Energy 6 (2021) 506–516.
[4] X. Huang, R. Zhou, X. Luo, X. Yang, J. Cheng, J. Yan, Experimental research and multi-physical modeling progress of Zinc-Nickel single flow battery: a critical review, Adv. Appl. Energy 12 (2023) 100154.
[5] O.J. Guerra, J. Zhang, J. Eichman, P. Denholm, J. Kurtz, B.M. Hodge, The value of seasonal energy storage technologies for the integration of wind and solar power, Energy Env. Sci. 13 (2020) 1909–1922.
[6] C. Yang, T. Wang, H. Chen, Theoretical and technological challenges of deep underground energy storage in China, Engineering 25 (2023) 168–181.
[7] Y. Balali, S. Stegen, Review of energy storage systems for vehicles based on technology, environmental impacts, and costs, Renew. Sustain. Energy Rev. 135 (2021) 110185.
[8] H. Riazi, T. Murphy, G.B. Webber, R. Atkin, S.S.M. Tehrani, R.A. Taylor, Specific heat control of nanofluids: a critical review, Int. J. Therm. Sci. 107 (2016) 25–38.
[9] S. Pourhemmati, S. Hossainpour, S.Z. Haeri, Experimental and numerical investigation of packed-bed thermal energy storage utilizing two phase change materials (PCM) in spherical capsules, Int. J. Therm. Sci. 210 (2025) 109605.
[10] H.M. Ali, T.u. Rehman, M. Arıcı, Z. Said, B. Duraković, H.I. Mohammed, R. Kumar, M.K. Rathod, O. Buyukdagli, M. Teggar, Advances in thermal energy storage: fundamentals and applications, Prog. Energy Combust. Sci. 100 (2024) 101109.
[11] L.B. Cédric, M. Anas, B. Ryad, S. Alain, Effect of Biot and Stefan numbers of a phase change material submitted to cyclic Robin conditions on the heat flux discharge, Int. J. Therm. Sci. 205 (2024) 109280.
[12] N. Zhang, L. Li, Z. Zhang, H. Köten, X. Lü, Y. Yuan, Effect of partially filled copper foam on the thermal performance of phase change materials under different direction external forces, Appl. Therm. Eng. (2025) 126814.
[13] Z. Liu, X. Gao, X. Huang, Y. Xie, J. Gao, X. Yang, Q. He, Evaluation on solar-biogas heating system for buildings: thermal characteristics and role of heat storage sectors, Appl. Energy 390 (2025) 125817.
[14] D. Zhu, Y. Han, T. Xu, L. Zhong, Y. Du, Development and characterization of new phase change concrete based on different composite phase change materials, Sol. Energy Mater. Sol. Cells 288 (2025) 113629.
[15] Z. Li, Y. Lu, R. Huang, J. Chang, X. Yu, R. Jiang, X. Yu, A.P. Roskilly, Applications and technological challenges for heat recovery, storage and utilisation with latent thermal energy storage, Appl. Energy 283 (2021) 116277.
[16] A. Anagnostopoulos, M.E. Navarro, Z. Jiang, Y. Ding, Enhancing composite phase change material thermal performance by tuning phase change materials properties with nanoparticles, Sol. Energy Mater. Sol. Cells 288 (2025) 113615.
[17] G. Wang, Z. Tang, Y. Gao, P. Liu, Y. Li, A. Li, X. Chen, Phase change thermal storage materials for interdisciplinary applications, Chem. Rev. 123 (2023) 6953–7024.
[18] A.V. Wilchinsky, S.A. Fomin, T.J.I.J.O.H. Hashida, m. transfer, contact melting inside an elastic capsule, 45 (2002) 4097–4106.
[19] Y. Zhao, W. Chen, F. Sun, Study on contact melting inside an elliptical tube with nonisothermal wall, (2009).
[20] T. Hirata, Y. Makino, Y. Kaneko, Analysis of close-contact melting for octadecane and ice inside isothermally heated horizontal rectangular capsule, Int. J. Heat. Mass Transf. 34 (1991) 3097–3106.
[21] J. Zhao, J. Zhai, Y. Lu, N. Liu, Theory and experiment of contact melting of phase change materials in a rectangular cavity at different tilt angles, Int. J. Heat. Mass Transf. 120 (2018) 241–249.
[22] A. Boroojerdian, H. Nemati, E. Selahi, Direct and non-contact measurement of liquid fraction in unconstrained encapsulated PCM melting, Energy 284 (2023) 129359.
[23] V. Chaurasiya, A. Wakif, N.A. Shah, J. Singh, A study on cylindrical moving boundary problem with variable thermal conductivity and convection under the most realistic boundary conditions, Int. Commun. Heat Mass Transf. 138 (2022) 106312.
[24] V. Chaurasiya, J. Singh, An analytical study of coupled convective heat and mass transfer with volumetric heating describing sublimation of a porous body under most sensitive temperature inputs: application of freeze-drying, Int. J. Heat. Mass Transf. 214 (2023) 124294.
[25] N. Hu, L.W. Fan, Close-contact melting of shear-thinning fluids, J. Fluid. Mech. 968 (2023) A9.

[26] S.A.A. Mehrjardi, A. Khademi, Z. Said, S. Ushak, A.J. Chamkha, Enhancing latent heat storage systems: the impact of PCM volumetric ratios on energy storage rates with auxiliary fluid assistance, Energy Nexus. 11 (2023) 100227.
[27] E. Assis, L. Katsman, G. Ziskind, R. Letan, Numerical and experimental study of melting in a spherical shell, Int. J. Heat. Mass Transf. 50 (2007) 1790–1804.
[28] S.F. Hosseinizadeh, A.A.R. Darzi, F.L. Tan, Numerical investigations of unconstrained melting of nano-enhanced phase change material (NEPCM) inside a spherical container, Int. J. Therm. Sci. 51 (2012) 77–83.
[29] Y. Kozak, G. Ziskind, Novel enthalpy method for modeling of PCM melting accompanied by sinking of the solid phase, Int. J. Heat. Mass Transf. 112 (2017) 568–586.
[30] M. Ezra, Y. Kozak, The influence of thermal convection in the thin molten layer on close-contact melting processes, Int. J. Heat. Mass Transf. 235 (2024) 126184.
[31] Z.R. Li, N. Hu, L.W. Fan, Nanocomposite phase change materials for high-performance thermal energy storage: a critical review, Energy Storag. Mater. 55 (2023) 727–753.
[32] A. Abdi, H. Rastan, Experimental comparative analysis of close-contact and constrained melting of n-eicosane in a finned rectangular cavity, Appl. Therm. Eng. 219 (2023) 119677.
[33] S. He, W. Wang, L. Wei, J. Ding, Heat transfer enhancement and melting behavior of phase change material in a direct-contact thermal energy storage container, J. Energy Storage 31 (2020) 101665.
[34] N. Hu, Z.R. Li, Z.W. Xu, L.W. Fan, Rapid charging for latent heat thermal energy storage: a state-of-the-art review of close-contact melting, Renew. Sustain. Energy Rev. 155 (2022) 111918.
[35] H.I. Mohammed, P. Talebizadehsardari, J.M. Mahdi, A. Arshad, A. Sciacovelli, D. Giddings, Improved melting of latent heat storage via porous medium and uniform joule heat generation, J. Energy Storage 31 (2020) 101747.
[36] M. Iasiello, M. Mameli, S. Filippeschi, N. Bianco, Metal foam/PCM melting evolution analysis: orientation and morphology effects, Appl. Therm. Eng. 187 (2021) 116572.
[37] W. Fu, X. Yan, Y. Gurumukhi, V.S. Garimella, W.P. King, N. Miljkovic, High power and energy density dynamic phase change materials using pressure-enhanced close contact melting, Nat. Energ. 7 (2022) 270–280.
[38] Z.R. Li, N. Hu, J. Liu, R.H. Zhang, L.W. Fan, Revisiting melting heat transfer of nano-enhanced phase change materials (NePCM) in differentially-heated rectangular cavities using thermochromic liquid crystal (TLC) thermography, Int. J. Heat. Mass Transf. 159 (2020) 120119.
[39] B. Xu, X. Zhao, X. Zuo, H. Yang, Progress of phase change materials in solar water desalination system: a review, Sol. Energy Mater. Sol. Cells 271 (2024) 112874.
[40] W. Wu, Y. Du, H. Qian, H. Fan, Z. Jiang, X. Zhang, S. Huang, Enhancing the waste heat utilization of industrial park: a heat pump-centric network integration approach for multiple heat sources and users, Energy Convers. Manage 306 (2024) 118306.
[41] Z. Zhang, Y. Chen, T. Ma, H. Tian, J. Liu, M. Zhou, W. Wang, Multi-type energy storage expansion planning: a review for high-penetration renewable energy integration, Renew. Sustain. Energy Rev. 219 (2025) 115853.
[42] X. Huang, Z. Li, Y. Xie, J. Gao, X. Yang, M.J. Li, Thermo-fluidic characteristics of contact melting mechanism for water-phase change material mixture: a numerical optimization, Int. J. Heat. Fluid. Flow. 110 (2024) 109561.
[43] N. Modi, X. Wang, M. Negnevitsky, Melting and solidification characteristics of a semi-rotational eccentric tube horizontal latent heat thermal energy storage, Appl. Therm. Eng. 214 (2022) 118812.
[44] X. Huang, F. Li, J. Guo, Y. Li, R. Du, X. Yang, Y.L. He, Design optimization on solidification performance of a rotating latent heat thermal energy storage system subject to fluctuating heat source, Appl. Energy 362 (2024) 122997.
[45] M.A. Dekhil, J.V. Simo Tala, O. Bulliard-Sauret, D. Bougeard, Numerical analysis of the performance enhancement of a latent heat storage shell and tube unit using finned tubes during melting and solidification, Appl. Therm. Eng. 192 (2021) 116866.
[46] V. Chaurasiya, S. Upadhyay, K.N. Rai, J. Singh, A temperature-dependent numerical study of a moving boundary problem with variable thermal conductivity and convection, Waves Random. Complex Media (2023) 1–25.
[47] V.R. Voller, C. Prakash, A fixed grid numerical modelling methodology for convection-diffusion mushy region phase-change problems, Int. J. Heat. Mass Transf. 30 (1987) 1709–1719.
[48] V. Safari, B. Kamkari, K. Hooman, J.M. Khodadadi, Sensitivity analysis of design parameters for melting process of lauric acid in the vertically and horizontally oriented rectangular thermal storage units, Energy 255 (2022) 124521.
[49] X. Huang, F. Li, Y. Li, X. Yang, M.J. Li, Solar photothermal utilization of coupled latent heat storage: a numerical and optimization study, Sol. Energy Mater. Sol. Cells 271 (2024) 112864.
[50] L.D. Landau, Fluid Mechanics, Course Of Theoretical Physics, 6, Addison-Wesley Publishing Co., 1959.
[51] S. Wang, Y. Shen, CFD-DEM-VOF-phase diagram modelling of multi-phase flow with phase changes, Chem. Eng. Sci. 273 (2023) 118651.
[52] A.F. Elmozughi, L. Solomon, A. Oztekin, S. Neti, Encapsulated phase change material for high temperature thermal energy storage – Heat transfer analysis, Int. J. Heat. Mass Transf. 78 (2014) 1135–1144.
[53] M. Ishii, T.C. Chawla, Local Drag Laws in Dispersed Two-Phase Flow, Argonne National Lab., IL (USA), 1979.
[54] N.G. Deen, J.A.M. Kuipers, Direct numerical simulation of fluid flow accompanied by coupled mass and heat transfer in dense fluid–particle systems, Chem. Eng. Sci. 116 (2014) 645–656.